frontiers | Frontiers in Earth Science

TYPE Original Research
PUBLISHED 10 October 2022
DOI 10.3389/feart.2022.916107

OPEN ACCESS

EDITED BY
Ryan Mathur,
Juniata College, United States

REVIEWED BY
Zhaochong Zhang,
China University of Geosciences, China
Behzad Mehrabi,
Kharazmi University, Iran

*CORRESPONDENCE
Frederik Börner,
frederik.boerner@fau.de

SPECIALTY SECTION
This article was submitted to Economic Geology,
a section of the journal
Frontiers in Earth Science

RECEIVED 08 April 2022
ACCEPTED 15 August 2022
PUBLISHED 10 October 2022

CITATION
Börner F, Keith M, Bücker JL, Voudouris P, Klemd R, Haase K, Kutzschbach M and Schiperski F (2022), In-situ trace element and S isotope systematics in pyrite from three porphyry-epithermal prospects, Limnos Island, Greece.
Front. Earth Sci. 10:916107.
doi: 10.3389/feart.2022.916107

In-situ trace element and S isotope systematics in pyrite from three porphyry-epithermal prospects, Limnos Island, Greece

Frederik Börner[1]*, Manuel Keith[1], Jonas L. Bücker[1], Panagiotis Voudouris[2], Reiner Klemd[1], Karsten Haase[1], Martin Kutzschbach[3] and Ferry Schiperski[3]

[1]Friedrich-Alexander-Universität (FAU) Erlangen-Nürnberg, GeoZentrum Nordbayern, Erlangen, Germany, [2]Faculty of Geology and Geoenvironment, National and Kapodistrian University of Athens, Athens, Greece, [3]Technische Universität Berlin, Institut für Angewandte Geowissenschaften, Berlin, Germany

Porphyry-epithermal systems associated with high-K calc-alkaline to alkaline igneous host rocks may be prospective for the recovery of Te among related elements like Cu, Ag, and Au. Limnos Island, as part of the Tethyan magmatic belt, is such an example, where (telescoped) porphyry-epithermal mineralization is accompanied by different alteration-styles reflecting various hydrothermal processes. Here, we present *in-situ* S isotope and trace element data of pyrite, which records the fluid evolution from the early porphyry to the late epithermal stage in three distinct prospects (Fakos, Kaspakas, Sardes) on Limnos Island. Pyrite in the sericitic alteration of Fakos mainly formed from single-phase magma-derived fluids lacking evidence for phase separation, as reflected by relatively constant $\delta^{34}S$ (about −4‰) and Co/Ni (0.1-1) values. By contrast, in the sericitic alteration of Kaspakas and the following epithermal stages, an influence of boiling is implied by negative $\delta^{34}S$ values to −15‰, significant intergrain $\delta^{34}S$ variations (>3‰), highly variable Co/Ni (100-0.01) and As/Co (10-0.001) in pyrite. Higher $\delta^{34}S$ values (above −4‰) in porphyry pyrite from Sardes and partly in the other two hydrothermal systems are related to mixing between magmatic S, and S which was transported through deeply circulated seawater and/or meteoric water. We propose that fluid-rock interaction buffered the pH to higher values, which enhanced the solubility of Au and Te. Subsequent boiling processes caused the Au deposition, whereas Te partitioned into the vapor and finally precipitated upon condensation into meteoric water. This process is accompanied by continuous cooling during fluid ascent from 780°C to <300°C, as indicated by increasing Sb, Tl, and Pb in pyrite from the porphyry to the epithermal stage. Consequently, the *in situ* $\delta^{34}S$ and trace element analysis allows to constrain the depositional environment of economic metals like Au and Te in porphyry-epithermal prospects.

KEYWORDS

tellurium–Te, telescoped porphyry-epithermal, *in-situ* d34S analysis, pyrite, LA-ICP-MS, Limnos Island

1 Introduction

Porphyry-epithermal ore deposits are the most important sources for Cu, Mo, Au, Ag, Sn, and W (Seedorff et al., 2005; Simmons et al., 2005; Sillitoe, 2010; Cheng et al., 2018; Liu et al., 2021). Some of these deposits are associated with alkaline igneous rocks in post-subduction settings and represent an economically important sub-class of this deposit-type due to a significant enrichment in Au, Ag, Te, and platinum group elements (Jensen and Barton, 2000; Kelley and Spry, 2016; Cheng et al., 2018; McFall et al., 2018; Liu et al., 2021). Prominent examples of alkaline-hosted Au-Ag-Te porphyry-epithermal deposits are Porgera and Ladolam, Papua New Guinea (Richards and Kerrich, 1993; Sykora et al., 2018), Vatukoula, Fiji (Pals and Spry, 2003; Börner et al., 2021), and Cripple Creek, Colorado (Kelley and Spry, 2016; Keith et al., 2020). Porphyry-epithermal mineralization associated with high-K calc-alkaline to shoshonitic and alkaline igneous rocks also occur in Europe, for example, as part of the Tethyan metallogenic belt (Marchev et al., 2005; Wallier et al., 2006; Fornadel et al., 2012; McFall et al., 2018; Voudouris et al., 2019a). These mineralizations may hold yet underestimated resources of critical raw materials like Te for sustainable energy production (Voudouris et al., 2019a). However, the ore-forming processes in porphyry-epithermal systems that are genetically and spatially linked to high-K calc-alkaline to alkaline magmatic activity are still poorly constrained (Richards, 2011; Smith et al., 2017; Keith et al., 2020; Börner et al., 2021).

Magmas in post-subduction settings are derived from the subcontinental lithospheric mantle that was previously metasomatized during arc magmatism, possibly leading to an enrichment in chalcophile elements and a high ore-forming potential (Richards, 2011; Holwell et al., 2019). The water-rich (≥4 wt.%) and oxidized (ΔFMQ = 0 to +2) character of these magmas enhances the partitioning of metals into exsolving magmatic fluids, which may feed porphyry-epithermal systems in the upper crust (Sillitoe, 2010; Lee et al., 2012; Vigneresse et al., 2019; Richards, 2022). High-K calc-alkaline to alkaline igneous rocks that host a hydrothermal system have a high capacity to buffer the fluid pH towards higher values due to fluid-rock interaction (Kouzmanov and Pokrovski, 2012; Smith et al., 2017). For instance, the disproportionation of magmatic SO_2 accompanying the ascent of magma-derived fluids would normally lead to fluid and host rock acidification (Ohmoto and Lasaga, 1982; Kouzmanov and Pokrovski, 2012). Instead, fluid-host rock buffering in alkaline porphyry-epithermal systems suppresses the pH decrease, leading to decreasing solubilities of Cl-complexed elements upon cooling, such as Co, Ni, and Cu (Heinrich, 2005; Kouzmanov and Pokrovski, 2012). By contrast, increasing fluid pH commonly enhances the solubility of Au and Te (Heinrich, 2005; Kouzmanov and Pokrovski, 2012; Grundler et al., 2013), which may be related to the formation of Au-Te rich mineralizations in alkaline-hosted environments (Zhang and Mao, 1995; Smith et al., 2017; Keith et al., 2020; Börner et al., 2021). Fluid-rock interaction and mineral precipitation lead to the formation of typical porphyry-epithermal alteration-styles, including calcic-sodic, potassic, sericitic, and advanced argillic (Sillitoe, 2010). Continuous cooling, crystallization and the retreat of the magma body accompanied by surface erosion or caldera collapse lead to telescoping (Sillitoe, 1994), i.e. overprinting of alteration zones that otherwise occur at distinct depth levels, which may cause an epithermal overprint in porphyry systems (Heinrich, 2005; Sillitoe, 2010).

Depending on the emplacement depth and degree of cooling, magmatic fluids may represent a single-phase supercritical liquid or comprise a low-density vapor and a high-density hypersaline liquid (>26 wt.% NaCl equivalent). Such fluids are typically related to lithostatic pressure conditions and may be ore-forming as part of the potassic alteration zone (Heinrich, 2005; Kouzmanov and Pokrovski, 2012). During ascent and cooling, the fluids pass the lithostatic-hydrostatic transition in the sericitic alteration zone, above which boiling and fluid mixing (including vapor condensation into meteoric fluids or seawater) are additional mechanisms of ore formation, which, besides mechanisms like conductive cooling, are particularly important in the epithermal environment (Hedenquist and Richards, 1998; Heinrich, 2005; Sillitoe, 2010; Kouzmanov and Pokrovski, 2012; Blundy et al., 2015). The combination of these processes leads to the typical bell-shaped mineralization and alteration in porphyry-epithermal systems, and is well documented by fluid inclusions hosted by the gangue mineralogy (Heinrich, 2005; Hurtig et al., 2021). However, fluid inclusions may not always report on the composition of the actual ore-forming fluids, to which the sulfides and the enrichment in critical elements is related (Redmond et al., 2004; Landtwing et al., 2005; Redmond and Einaudi, 2010). How these processes are preserved by the trace element and S isotope signature of hydrothermal sulfides is still debated and poorly investigated in the porphyry environment (Deditius et al., 2011; Reich et al., 2013; Hutchison et al., 2020; Eldridge et al., 2021; González-Jiménez et al., 2021).

We present a detailed study on the trace element and S isotope composition of pyrite from three distinct (telescoped) porphyry-epithermal prospects associated with high-K calc-alkaline and shoshonitic igneous rocks on Limnos Island, Greece. The close spatial and temporal relation of these three prospects makes it an ideal natural laboratory to study the fractionation processes of Te and related elements (e.g., Au, Ag) in the porphyry-epithermal environment.

2 Geological overview

The northern Aegean Sea, where Limnos Island is located, is part of the Tethyan orogenic belt. This segment of the

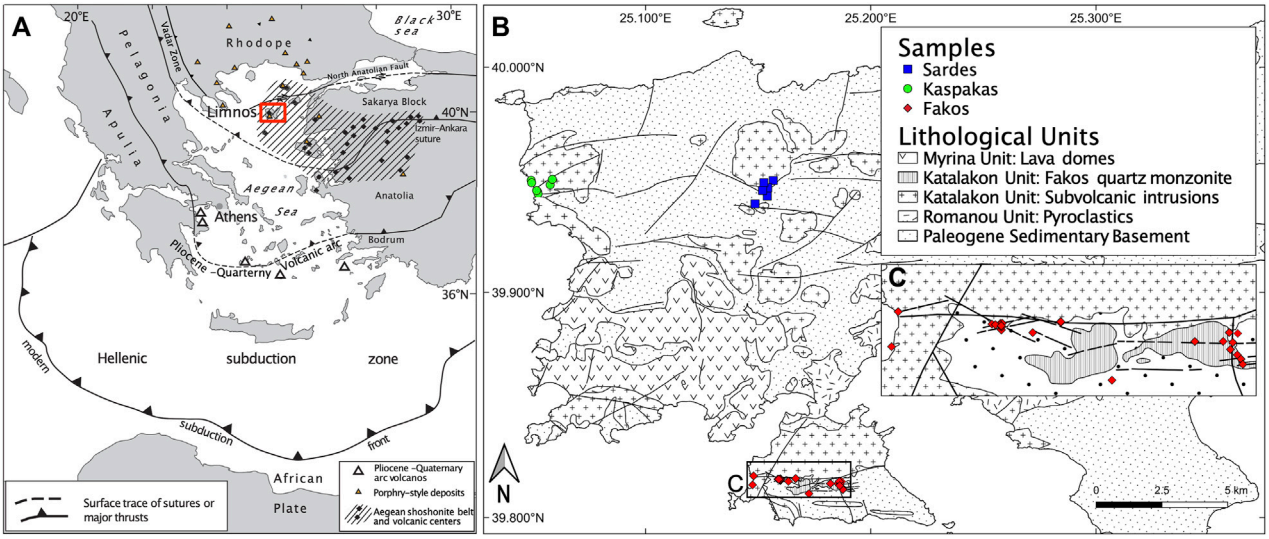

FIGURE 1
(A) Geographical overview, major tectonic units and porphyry-style deposits in the Aegean region. Modified after Pe-Piper et al. (2009), Baker (2019) and Voudouris et al. (2019b). The red rectangle outlines the location of Limnos Island in the Aegean shoshonite belt. **(B)** Simplified geological map of Limnos Island highlighting the different lithological units after Innocenti et al. (1994) and Pe-Piper et al. (2009). The different porphyry-epithermal systems and related sample locations (Table 1) are presented by the red diamonds (Fakos), green circles (Kaspakas), and blue squares (Sardes); **(C)** Detailed map of Fakos.

Alpine-Himalayan deformational belt extends eastward from Greece into Turkey and formed as a result of plate convergence between Africa and Eurasia. The Tethyan orogenic belt consists of three continental blocks (Rhodope, Pelagonia and Apulia) separated by fragments of oceanic crust (Vardar-Izmir and Pindos basins). These have been subject to nappe stacking and thrusting from late Cretaceous to Cenozoic time (van Hinsbergen et al., 2005; Jolivet and Brun, 2010; Ring et al., 2010). The subduction of the Vardar Ocean beneath the Rhodopes and the accretion of Pelagonia resulted in low temperature/high pressure metamorphism under blueschist to low eclogite facies conditions (e.g., Okrusch and Bröcker, 1990; Ring and Layer, 2003). Ongoing subduction during the Cenozoic led to the accretion of the Pindos Ocean followed by the subduction and accretion of Apulia in the late Eocene to early Miocene (Sotiropoulos et al., 2003; Ring et al., 2010). Besides the compressional evolution of the Aegean region, large scale back-arc extension occurred in response to slab roll-back and syn- to post-orogenic collapse of the Tethyan orogenic belt during late Mesozoic and Cenozoic time (Figure 1A; Jolivet and Brun, 2010; Ring et al., 2010; Menant et al., 2018). Igneous activity related to the southward migration of the subduction zone commenced in the late Cretaceous with the development of a volcanic arc in the Balkan region (Fytikas et al., 1980; De Boorder et al., 1998; Kilias and Mountrakis, 1998; Pe-Piper et al., 1998; Melfos et al., 2002), whereas the active volcanic arc lies in the south Aegean Sea (Figure 1A; Fytikas et al., 1984; Pe-Piper and Piper, 2002). Large amounts of sedimentary and continental material were subducted into the upper mantle. This possibly caused diapiric ascent from the slab and contributed to the high-K to shoshonitic magmatism in the northern Aegean region (Schaarschmidt et al., 2021a) that is associated with porphyry and epithermal mineralizations, such as those on Limnos Island (Figure 1; Gläser et al., 2022).

The geology of Limnos Island consists of Paleogene sediments that are partly overlain and intruded by three Miocene volcanic to subvolcanic units (Myrina, Romanou and Katalakon) (Figure 1B). The Paleogene sediments originate from the Rhodope orogen and were deposited into the North Aegean Trough, which was formed by post-orogenic collapse and extension (Bonev and Beccaletto, 2007; Caracciolo et al., 2011). The oldest sediments are of middle to late Eocene age and consist of turbidites and tuffs, while the younger sediments are interbedded marine to shallow marine sandstones, conglomerates, and marls. The onset of continental sedimentation in the early Miocene marks an abrupt change after a deformational and erosional phase (Innocenti et al., 2008). The igneous rocks on Limnos Island formed from ~22.3 to 18 Ma and unconformably overlay the Paleogene sedimentary basement (Figure 1B; Fytikas et al., 1980; Roussos, 1993; Innocenti et al., 1994; Pe-Piper et al., 2009). The magmas show a subduction zone signature, influenced by fluids released from subducted sediments and lack evidence for crustal assimilation (Gläser et al., 2022). The igneous complex consists of hypabyssal intrusions, domes, lavas, and pyroclastic flows of high-K calc-alkaline to shoshonitic composition (Figure 1B; Gläser et al.,

2022), which were subdivided into three volcanic units by Innocenti et al. (1994): 1) The Romanou unit (22.3 ± 0.7 Ma; Pe-Piper et al., 2009) consists of pyroclastic sequences and strombolian-type deposits of trachy-basaltic andesitic to rhyolitic composition (Pe-Piper et al., 2009). Continental sediments with abundant plant remnants, silicified wood, and silica associated with hot spring activity accompany the volcanic rocks of this unit (Figure 1B; Innocenti et al., 1994; VoudourisVelitzelos et al., 2007). 2) The Katalakon unit (21.3–20.2 Ma; Fytikas et al., 1980; Innocenti et al., 1994) cross-cuts the older Romanou unit and is exposed along a NW-SE trending zone in the western part of the island. Subvolcanic rocks of andesitic to dacitic composition dominate this unit together with a quartz-monzonite body that is exposed on the Fakos peninsula (Innocenti et al., 1994). 3) The Myrina unit (17.9–19.3 Ma; Fytikas et al., 1980) is separated from the Katalakon unit by NW-SE and N-S trending faults (Innocenti et al., 1994). Porphyritic dacites form lava domes and flows that occur in association with monogenic breccias and lahars (Innocenti et al., 1994). The tectonic evolution of Limnos Island is represented by an early compression, followed by different extensional phases (Roussos, 1993; Innocenti et al., 1994). Normal faults striking NE-SW and E-W are the dominant fault types on Limnos, which cross-cut both the sedimentary sequence and the igneous complexes (Figures 1B,C; Tranos, 2009).

The ~20 Ma old Fakos quartz-monzonite in south-western Limnos was emplaced into Middle to Upper Eocene sandstones forming a Paleogene sedimentary basement and into Lower Miocene shoshonitic subvolcanic rocks of the lower Katalakon unit (Voudouris, 2006; Innocenti et al., 2008). Associated with the quartz-monzonite are multi-stage veins and mineralizations of a telescoped porphyry Cu and epithermal Au-Te system (Voudouris, 2006; Fornadel et al., 2012). Hydrothermal fluids silicified the sandstones around the intrusion center and locally introduced finely disseminated pervasive sulfides (Fornadel et al., 2012). Late E-W striking dikes of shoshonitic composition cross-cut the monzonite and other volcanic units (Voudouris, 2006; Kamvisis, 2019). The epithermal mineralization at Fakos is closely related to E-W trending fault zones (Figure 1B; Fornadel et al., 2012). The Kaspakas prospect is located in northwestern Limnos and is hosted in volcanic to subvolcanic rocks of the Katalakon unit (Figure 1B). The telescoped porphyry-epithermal system comprises quartz stockworks, which are cross-cut by quartz-tourmaline-carbonate veins with base metal sulfides (Voudouris et al., 2019b). The Sardes prospect is located in the central part of the island and comprises volcanic- to subvolcanic- and sediment-hosted mineralizations. The host rocks are part of the Katalakon unit and the Paleogene Sedimentary Basement (Figure 1B). Early porphyry-style mineralization is related to a sodic-calcic/potassic alteration assemblage followed by a later sericitic alteration including tourmaline veins (Voudouris et al., 2019b). Epithermal veins overprint both the altered subvolcanic rocks and the sediments that occur in close spatial relation to the porphyry system (Voudouris et al., 2019b).

3 Methods

3.1 Samples and bulk rock analysis

Two sets of samples were investigated in this study, namely the LM series (Kaspakas n = 8; Sardes n = 6; Fakos n = 9) and the LM-JB series (Fakos n = 19, Tables 1–3). From these samples, a total of 17 polished thin sections were prepared at the University of Würzburg and 23 polished blocks were prepared at the University of Hamburg. A total of 17 representative samples from Fakos were crushed and milled to a homogenous powder for their mineralogical analysis by a Siemens D5000 X-ray diffractometer at the GeoZentrum Nordbayern (Supplementary Table S3). The data was processed using the Rietveld-algorithm with the Profex software package, which allowed a quantification of mineral abundances >1 wt.% (Doebelin and Kleeberg, 2015).

3.2 Major and trace element micro-analysis

The polished blocks and thin sections were examined by optical and electron microscopy for mineral phase identification at the GeoZentrum Nordbayern. A Tescan VEGA II XMU and a Hitachi TM 4000 scanning electron microscope equipped with an Oxford Instruments EDS detector were used at acceleration voltages of 15 kV or 20 kV to identify the unknown mineral phases.

Major and trace element mapping by a Bruker M4 Tornado µ-XRF was performed on six polished blocks (Kaspakas = 5; Sardes =1, Table 3) at the MAGMA Lab of the TU Berlin, aiming to quantify the main mineral phases. The instrument is equipped with an X-ray focusing capillar optic and two 30 mm^2 silicon drift detectors. Mappings were performed using a 20 µm spot size. The Rh-anode was operated at 50 kV acceleration voltage and an anode current of 600 mA at a chamber vacuum of 20 mbar. Spots were set at intervals of 20 µm and measured for 90 ms yielding a total mapping time of about 24 h per polished block. Element quantification was performed by a standardless method (Flude et al., 2017). The energy position of the fluorescence lines and the power of the X-ray tube are calibrated monthly, using a set of single element standards provided by Bruker (Germany). Since small intergrowth of different minerals in alteration assemblages (e.g., feldspar and sericite) are common, the threshold for assigning a chemical composition by µ-XRF analysis to certain minerals was broadened. This may result in an underestimation

TABLE 1 Compilation of the Fakos epithermal transitional and Fakos porphyry samples investigated in this study with respect to sample, sampling site, alteration type, mineralogy and applied analytical techniques.

Symbol	Latitude/ Longitude	Sample ID	Alteration host-rock and ore minerals	polished section	XRD	EPMA	µ-RFA	LA-ICP-MS	δ34S LA-ICP-MS
Fakos—porphyry									
◆	N 39.81498°/E 25.18641°	LM-64	Porphyry, sericitic altered monzonite, overprinting potassic alteration with py in veinlets, minor mol, rt, sp and cpy	x		x		py (30), sp (3)	6
◆	N 39.81413°/E 25.18622°	LEM-81	Porphyry, potassic ore minerals: cpy, hem, mag	x					
◆	N 39.81306°/E 25.18736°	LM-84	Porphyry, potassic altered monzonite, massive magnetite vein, ore minerals: mag, hem, ±cpy, ±py	x					
◆	N 39.81615°/E 25.18600°	LEM-87	Porphyry, potassic ore minerals: cpy, hem, mag	x					
◆	N 39.81509°/E 25.18205°	LM-97B	Porphyry, potassic, cf. LM-84, ore minerals: py, cpy, hem, mag	x					
◆	N 39.81651°/E 25.15975°	LM-JB-04	Porphyry, altered monzonite dyke with oxidized stockwork veinlets		x				
◆	N 39.81641°/E 25.15987°	LM-JB-05	Porphyry, strongly altered and weathered; brecciated quartz vein		x				
◆	N 39.81510°/E 25.18531°	LM-JB-17	Porphyry, monzonite with feldspar destructive alteration (possibly overprinting potassic alteration) with fine quartz veinlets with ± mag, cpy	x	x				
◆	N 39.81355°/E 25.18694° (not outcropping)	LM-JB-18	Porphyry, potassic altered monzonite with irregular patches of mag cut by grey, fine grained qz veinlets	x	x				
◆	N 39.81602°/E 25.18699°	LM-JB-20	Porphyry, potassic monzonite with approx. 5 mm wide mag veinlets (M-type) ± cpy, py	x (2)	x				
Fakos—transitional (shallow porphyry)									
◇	N 39.81454°/E 25.14749°	LM-JB-03	Transitional, crustiform carbonate veins, cross-cutting sandstone with py, cpy, hem	x	x			py (18)	
◇	riverbed, not outcropping (ca.100m upstream of LM-JB-12)	LM-JB-11	Transitional, sandstone impregnated with fine py and gn						
◇	N 39.81738°/E 25.16660°	LM-JB-13	Transitional, sandstone cross-cut by fine tourmaline veins - veinlets; disseminated py	x	x				
◇	N 39.81737°/E 25.16664°	LM-JB-14	Transitional, sandstone cut by fine qz ±Fe-oxide veins - veinlets; disseminated py	x	x			py (14)	
◇	N 39.81064°/E 25.17252° (not outcropping)	LM-JB-16	Transitional, quartz-rich sandstone with stockwork veins - veinlets of tourmaline ore minerals		x				
◇	riverbed near LM-JB-18 (not outcropping)	LM-JB-19	Transitional, breccia cemented by tourmaline						
◇	N 39.81852°/E 25.14793°	LM-JB-01	Transitional, secondary altered volcanogenic rock with strongly altered clay mineral replacing primary texture ±hem		x				
◇	N 39.81852°/E 25.14793°	LM-JB-02	Transitional, secondary alteration, cf. LM-JB-01, ore minerals: hem		x				
◇	N 39.81611°/E 25.16341°	LM-JB-10	Transitional, strongly altered and weathered; primary mineral assemblage is completely replaced by clay minerals; altered stockwork veins - veinlets with alteration halos		x				

Mineral abbreviations after Whitney and Evans (2010), cf. Figure 2.

TABLE 2 Compilation of the Fakos HS and IS epithermal samples investigated in this study with respect to sample, sampling site, alteration type, mineralogy and applied analytical techniques.

Symbol	Longitude/ Latitude	Sample ID	Alteration host-rock and ore minerals	polished section	XRD	EPMA	µ-RFA	LA-ICP-MS	δ34S LA-ICP-MS
Fakos—HS epithermal									
◆	N 39.81701°/E 25.15912°	LM-29	HS Epithermal, brecciated py vein with massive silicification and qz veinlets; py, sp, en, tnt, gn	x		x		py (23), sp (10)	8
◆	N 39.81852°/E 25.14793°	LEM-88	Epithermal, advanced argillic alteration, disseminated py, ore minerals: py	x					
Fakos—IS epithermal									
◇	N 39.81675°/E 25.15980°	LM-27B	Epithermal, IS epithermal brecciated quartz veinlets cemented by milky and comb quartz; py, BMS, sulfosalts (bournonite, tetrahedrite) supergene: Fe-oxides + cov	x		x		sp (17), gn (3)	
◇	N 39.94583°/E 25.16148°	LM-89	Epithermal, IS epithermal carbonate veinlets, ore minerals: py, sp, gn	x				py (15), sp (2), gn (4)	9
◇	N 39.81702°/E 25.15967°	LM-33 (a,b)	Epithermal, IS epithermal quartz-carbonate veins with pyrite, BMS, tellurides and electrum hosted in intermediate argillic altered sandstones and lavas	x (2)		x (2)		py (20), sp (13), cpy (11), gn (6), sulfosalts	5
◇	N 39.81718°/E 25.15970°	LM-JB-06	Epithermal, quartz-carbonate veins - veinlets with BMS	x (2)	x			py (16), gn (2)	
◇	N 39.81709°/E 25.15872°	LM-JB-07	Epithermal, quartz-carbonate vein with BMS (gn, py) in contact zone between lamprophyric dyke and sandstone	x (4)				py (36), sp (9), cpy (5), gn (8)	
◇	N 39.81718°/E 25.15990°	LM-JB-09	Epithermal, silicified sandstone, hornfels, with a fine aphanitic texture and impregnated with fine, interstitial py						
◇	N 39.81725°/E 25.16662°	LM-JB-12	Epithermal, sandstone cut by quartz and tourmaline veinlets; oxidized Fe-bearing veinlets and py; nearby a large fault zone ore	x	x				
◇	riverbed (not outcropping) down stream of LM-JB-14	LM-JB-15	Epithermal, three samples: (a) and (b): sandstone with py; (c) altered monzonite cut by quartz vein	x (2)	x (3)				
◇	N 39.81852°/E 25.14793°	LM-JB-01	IS Epithermal, strongly altered with clay mineral replacing primary texture ±hem secondary alteration in volcanogenic rock		x				
◇	N 39.81852°/E 25.14793°	LM-JB-02	Epithermal, secondary alteration, cf. LM-JB-01, ore minerals: hem		x				
◇	N 39.81611°/E 25.16341°	LM-JB-10	Epithermal, strongly altered and weathered; primary mineral assemblage is completely replaced by clay minerals; altered stockwork veinlets with alteration halos		x				

Mineral abbreviations after Whitney and Evans (2010), cf. Figure 2.

of small grained minerals. Mineral quantification was carried out with ImageJ (Schneider et al., 2012).

The major and minor element composition of sulfides (pyrite, sphalerite, galena, and chalcopyrite) and sulfosalts (tennantite-tetrahedrite and bournonite) was determined by electron probe microanalysis (EPMA) using a JEOL JXA-8200 Superprobe at the GeoZentrum Nordbayern (Supplementary Table S2). The quantitative analysis was carried out in an evacuated chamber (<4.0 x 10^{-6} mbar) with a focused beam, an acceleration voltage of 20 kV and a beam current of 20 nA.

TABLE 3 Compilation of the investigated samples from Kaspakas and Sardes in this study with respect to sample, sampling site, alteration type, mineralogy and applied analytical techniques.

Symbol	Longitude/ Latitude	Sample ID	Alteration host-rock and ore minerals	polished section	XRD	EPMA	µ-RFA	LA-ICP-MS	δ34S LA-ICP-MS
Kaspakas - porphyry									
●	N 39.94979°/E 25.04916°	LEM-1	Porphyry, sericitic altered subvolcanic, ore minerals: py, po,	X			x	py (7)	
●	N 39.94871°/E 25.04940°	LEM-3BII	Porphyry, sericitic altered subvolcanic, ore minerals: py, cpy, po	X			x	py (8)	
●	N 39.94467°/E 25.05204°	LEM-7	Porphyry, sericitic altered subvolcanic in proximity to vein, ore minerals: py, po, hem	X			x	py (10)	9
Kaspakas—IS epithermal									
○	N 39.94524°/E 25.05160°	LEM-6	Epithermal, IS epithermal overprint of sericitic altered subvolcanic, ore minerals: py, sp, gn, po	X		x	x	py (16), sp (1)	
○	N 39.94386°/E 25.05224°	LEM-8	Epithermal, IS epithermal overprint of propylitic altered subvolcanic with epithermal overprint, ore minerals: py	X				py (8)	5
○	N 39.95022°/E 25.05858°	LEM-18	Epithermal, IS epithermal overprint of sericitic altered subvolcanic, ore minerals: py, cpy, sp, gn, hem	X		x	x	py (12)	6
○	N 39.94778°/E 25.05763°	LEM-19	Epithermal, IS epithermal carbonate vein cutting through subvolcanic, ore minerals: py, sp, gn	X		x		py (18), sp (14), gn (1)	5
Sardes - porphyry									
■	N 39.94647°/E 25.15424°	LEM-35	Porphyry, weakly potassic altered subvolcanic, cpy-mt-qtz veinlets, ore minerals: py, po, cpy	X		x		py (10)	3
■	N 39.94273°/E 25.15401°	LEM-40	Porphyry, sodic-calcic with potassic overprint, subvolcanic host-rock, A-type veinlets, ore minerals: py, cpy, mag	X				py (2), cpy (3)	
■	N 39.93930°/E 25.14858°	LEM-51	Porphyry, propylitic altered subvolcanic, ore minerals: py, po	X				py (7)	7
■	N 39.94972°/E 25.15664°	LEM-65	Porphyry, potassic altered subvolcanic, ore minerals: py, cpy, po, mag	X				py (8)	1
Sardes—epithermal									
□	N 39.94873°/E 25.15249°	LEM-33	Epithermal, silicified sandstone, ore minerals: py, mrc, apy	X		x		py (6), mrc (9)	1

Mineral abbreviations after Whitney and Evans (2010), cf. Figure 2.

Analyzed elements were Te, As, S, Cu, Cd, Au, Ag, Fe, Sb, Pb, and Zn, which refer to the following standards: $AgTe_2$ (Te, Ag), InAs (As), FeS_2 (Fe, S), $CuFeS_2$ (Cu), CdS (Cd), Au (Au), InSb (Sb), ZnS (Zn), and PbTe (Pb). The measurements were performed on the following peaks and spectroscopic crystals: Te (Lα, PETJ), Ag (Lα, PETJ), Fe (Kα, LIF), S (Kα, PETJ), Cu (Kα, LIF), Cd (Lα, PETH), Au (Mα, PETJ), Sb (Lβ, PETJ), Pb (Mα, PETJ), Zn (Kα, LIF). The chemical formulae of the tennantite-tetrahedrite solid solution series were calculated on the basis of 29 atoms (Supplementary Table S2), according to the method described by Marushchenko et al. (2018). Stoichiometric calculations of the cation sums were used for data quality assurance. Most analyses displayed an uncertainty with respect to the ideal stoichiometric composition of ≤1 at.%. Analysis with analytical totals <99 and >101 wt.% were discarded and K-raw (K-raw = unknown intensity for element A at λ/standard intensity for element A at λ) values of the analyzed elements on the respective standards in the range of ≥99 to ≤101% were accepted (Table 1).

Each spot analyzed by EPMA was marked on a back-scattered electron image for the subsequent analysis of the same mineral grain by LA-ICP-MS (n = 416) using the S content of the respective mineral as the internal standard. The trace element analysis was carried out by a Teledyne Analyte Excite 193 nm laser coupled with an Agilent 7500c quadrupole ICP-MS at the GeoZentrum Nordbayern (Supplementary Table S5). Helium was used as the carrier gas with a mass flow rate of 650–900 ml/min. A single spot ablation pattern with a frequency of 10–20 Hz, an irradiance of 0.77 GW/cm^2 and a fluence of

3–4 J/cm^2 was applied. A beam diameter of 25 µm was used and on occasion of 20 to 10 µm according to sulfide crystal size. Total run time was set to 60 s including 20 s of gas blank analysis prior to ablation. The reference material Po724 B2 SRM (Memorial University Newfoundland) was used for the external standardization of Au and MASS-1 for all other elements. The UQAC FeS-1 reference material (https://sulfideslasericpms.wordpress.com) was used as a secondary standard. Relative standard deviations (RSD) for most elements were <10%–15% (Supplementary Table S4). The sulfide standards were analyzed several times during an analytical day to monitor the instrument drift. Trace element concentrations and minimum detection limits (Supplementary Table S5) were processed with the Iolite software package developed at the University of Melbourne (https://iolite-software.com). Spikes in the time-resolved laser ablation spectra were excluded for the calculation of the trace element concentrations.

3.3 *In-situ* δ^{34}S analysis

The quantitative *in-situ* analysis of $^{34}S/^{32}S$ ratios was performed at the MAGMA Lab of the TU Berlin using a Teledyne Analyte Excite 193 nm excimer laser coupled to an Agilent 8900 ICP-MS/MS. Helium was used as the carrier gas at a total mass flow rate of 800 ml/min (Supplementary Table S6). The S isotopes were measured in mass shift mode using an O_2 filled reaction cell at O_2 flow rates of 0.165 ml/min to avoid interferences of molecular ions at m/z = 32 (e.g., $^{16}O^{16}O^+$ and $^{14}N^{18}O^+$) and m/z = 34 ($^{18}O^{16}O^+$and $^{15}N^{18}OH^+$). To maximize the spatial resolution, the analysis was performed in spot mode using a 50 µm spot size at a repetition rate of 10 Hz. The Balmat pyrite and sphalerite were used as primary and secondary δ^{34}S standards, respectively (Crowe and Vaughan 1996). The δ^{34}S values of the unknowns were corrected for instrumental mass bias (MB, Eq. 1) using the drift-corrected average δ^{34}S value of repeated measurements (n= 27-30) of the Balmat pyrite reference material ($\delta^{34}S_{measured(RM)}$). For $\delta^{34}S_{expected(RM)}$ the value 15.1 ± 0.2‰ from Crowe and Vaughan (1996) was used.

$$MB = \delta^{34}S_{measured\,(RM)} - \delta^{34}S_{excepted\,(RM)} \quad (1)$$

$$\delta^{34}S_{corr\,(sample)} = \delta^{34}S_{measured\,(sample)} - MB \quad (2)$$

Reproducibility was estimated for each session from the RSD of the drift-corrected measurements of $\delta^{34}S_{VCDT}$ in the Balmat pyrite divided by $\sqrt{n}$, which was <0.7‰. Measurements of the Balmat sphalerite resulted in $\delta^{34}S_{corr(sample)}$ values of 14.7 ± 1.6‰ (1 RSD_{mean}, n = 10, session 1) and 13.6 ± 1.7‰ (1 RSD_{mean}, n = 9, session 2) indicating a good accuracy and day-to-day reproducibility of the method. A full description of the analytical set is provided in the Supplementary Table S1.

4 Results

4.1 Alteration types

Samples from the different porphyry and epithermal stages (n = 40) were classified according to their alteration mineralogy by a combination of optical microscopy, µXRF, and XRD (Tables 1–3; Supplementary Table SA3). On this basis, the following mineralization-styles were defined for the three investigated prospects on Limnos Island (Figure 1B): 1) porphyry, transitional, high sulfidation (HS) epithermal, and intermediate sulfidation (IS) epithermal at Fakos, 2) porphyry and IS epithermal at Kaspakas, and 3) porphyry, IS epithermal, and low sulfidation (LS) epithermal at Sardes (Figures 2A–C). We note that the Sardes LS association likely represents fluctuations in the fluid condition of the IS epithermal stage or may be related to an overprint through a hydrothermal event at a later time.

4.1.1 Fakos

The quartz-monzonite hosts the early porphyry mineralization at Fakos (LM-JB-17 to -20), which comprises a potassic alteration assemblage dominated by biotite, magnetite and K-feldspar (Supplementary Table S3) followed by a sericitic alteration with abundant quartz veins (LM-64). In many of our samples it is unclear whether we see veinlets or veins. We will refer to those veinlets/veins as veins in the following, more detailed sample descriptions are provided in Tables 1 through 3. The transitional stage is characterized by sandstones that host tourmaline and hydrothermal quartz ± calcite in close spatial relation to fault zones crosscutting the Fakos quartz-monzonite (LM-JB-14; Figure 2A). At the western coast of the Fakos peninsula, dolomite, kaolinite, alunite, calcite, and sulfides in partially open veins occur as part of the transitional stage (LM-JB-03). These veins are commonly related to a large E-W trending fault zone (Figure 1C). Because properties of both, epithermal and porphyry alteration are present, the term transitional is adapted from Fornadel et al. (2012), however, shallow porphyry could be used as alternative terminology. The HS epithermal stage at Fakos (LM-29) consists of pale-brown feldspar associated with zones of massive silicification with milky quartz. The altered host rocks associated with mineralized veins of the IS epithermal stage (e.g., LM-JB-06) are dominated by quartz and white mica, as well as chlorite and/or plagioclase with local microcline and sanidine (Supplementary Table S3). Veins of the IS epithermal stage to the west of the Fakos quartz-monzonite relate to an approximately E-W striking dominantly quartz bearing fault zone that is hosted by siliciclastic sediments, and subvolcanic intrusions of the Katalakon unit (Figure 1C).

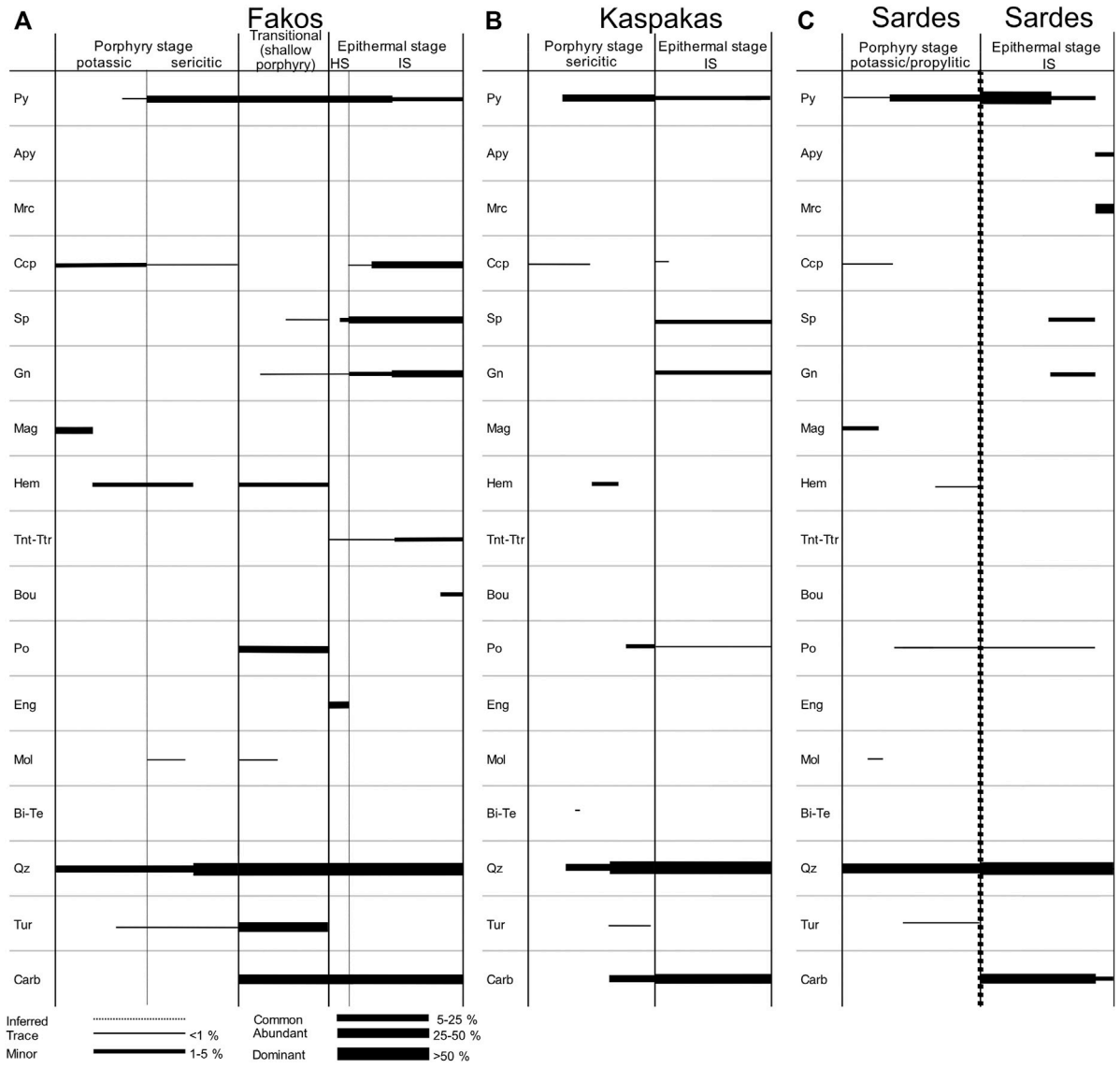

FIGURE 2
Paragenetic sequence of the three porphyry-epithermal system: **(A)** Fakos, **(B)** Kaspakas, and **(C)** Sardes. Note that the relation between Sardes porphyry and epithermal is unclear and therefore separated by a dashed line. Mineral abbreviations after Whitney and Evans (2010): py, pyrite; apy, arsenopyrite; mrc, marcasite; ccp, chalcopyrite; sp, sphalerite; gn, galena; mag, magnetite; hem, hematite; tnt-ttr, tetrahedrite-tennantite; bou, bournonite; po, pyrrhotite; eng, enargite; mol, molybdenite; qz, quartz; tur, tourmaline; carb, carbonate.

4.1.2 Kaspakas

At Kaspakas, the porphyry mineralization is hosted by subvolcanic andesites to dacites. The porphyry mineralization in the Kaspakas hydrothermal system is dominated by sericitic alteration (LEM-1, LEM-3, and LEM-7), as expressed by secondary quartz, sericite, orthoclase/microcline, tourmaline (and minor calcite) (Supplementary Data Sheet S2). The epithermal stage is hosted by subvolcanic rocks of andesitic to dacitic composition. The IS epithermal stage at Kaspakas is characterized by quartz and calcite veins, hosting base metal sulfides and tennantite-tetrahedrite (e.g., LEM-19).

4.1.3 Sardes

At Sardes, similar to Kaspakas, the porphyry mineralization is hosted by subvolcanic andesites to dacites. Porphyry samples from Sardes relate to an early stage of potassic alteration in close proximity to the porphyry center (LEM-35; LEM-40; LEM-65) and to a propylitic alteration assemblage in the distal parts of the system, which comprises epidote and chlorite (LEM-51). The

10.3389/feart.2022.916107

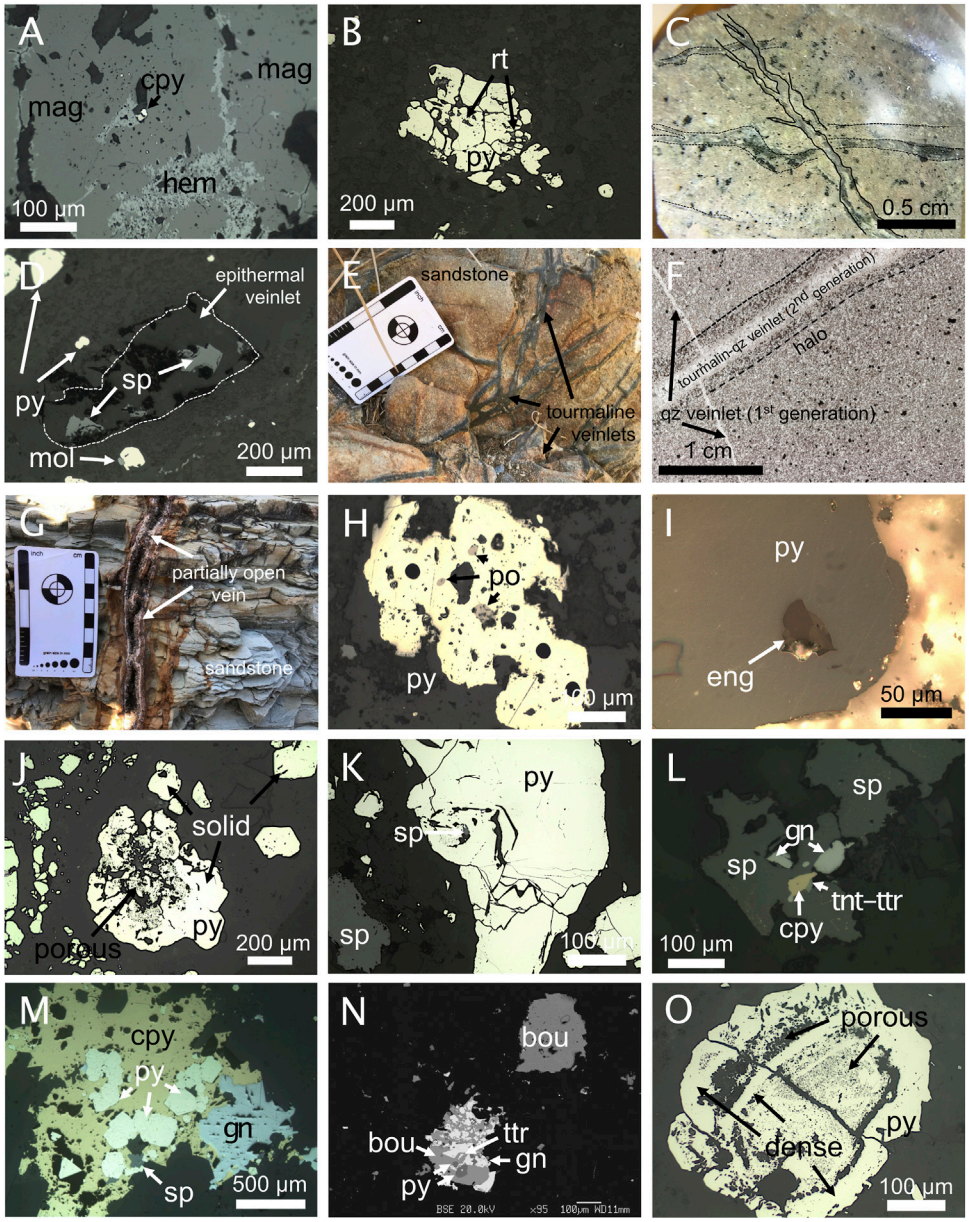

FIGURE 3
Field photographs, microphotographs and BSE image of Fakos samples: **(A)** Porphyry sample with chalcopyrite hosted by magnetite and hematite from the potassic alteration zone (LM-84); **(B)** Porphyry pyrite with rutile, LM-64; **(C)** Cross-cutting relationships of quartz veinlets in the porphyry stage, LM-64; **(D)** Porphyry pyrite and molybdenite from the sericitic alteration with later-stage epithermal sphalerite, we note that the crystal facets of the pyrites may partly only be visible under high magnification; **(E)** Cross-cutting relationships of sandstone-hosted transitional stage quartz-tourmaline veinlets (related samples: LM-JB-13, -14); **(F)** Scan of thin section with disseminated transitional pyrite in sandstone associated with tourmaline and different generations of quartz veinlets. Note that pyrite is absent in the alteration halos of 1st generation quartz vein. **(G)** Partially open veins with crustiform banding of carbonates and Fe-oxides in sandstones from the transitional stage, LM-JB-03; **(H)** Slightly porous pyrite (LM-JB-14) with pyrrhotite inclusions from the transitional stage; **(I)** Enargite in pyrite in cross polarized light from the epithermal HS stage, LM-29; **(J)** Pyrite with dense and porous domains with smaller dense pyrite crystals, LEM-29; **(K)** Dense slightly brecciated pyrite associated with sphalerite, LM-29; **(L)** Galena, chalcopyrite and tetrahedrite-tennantite associated with sphalerite hosting chalcopyrite inclusions from the epithermal IS stage, LM-27; **(M)** Pyrite surrounded by chalcopyrite followed by later-stage galena and sphalerite surrounding chalcopyrite in the epithermal IS stage, LM-33a; **(N)** Pyrite associated with galena, bournonite and Ag-rich tetrahedrite in back-scattered electron contrast, LM- 27B; **(O)** Pyrite with dense and porous domains from the epithermal HS stage, LEM-29. Further details about the investigated samples are presented in Table 1. Mineral abbreviations after Whitney and Evans (2010): Py, pyrite; Cpy, chalcopyrite; Sp, sphalerite; Gn, galena; Mag, magnetite; Hem, hematite; Tnt-Ttr, tetrahedrite-tennantite; Bou, bournonite; Po, pyrrhotite; Eng, enargite; Mol, molybdenite; Rt, Rutile; Qz, quartz.

10.3389/feart.2022.916107

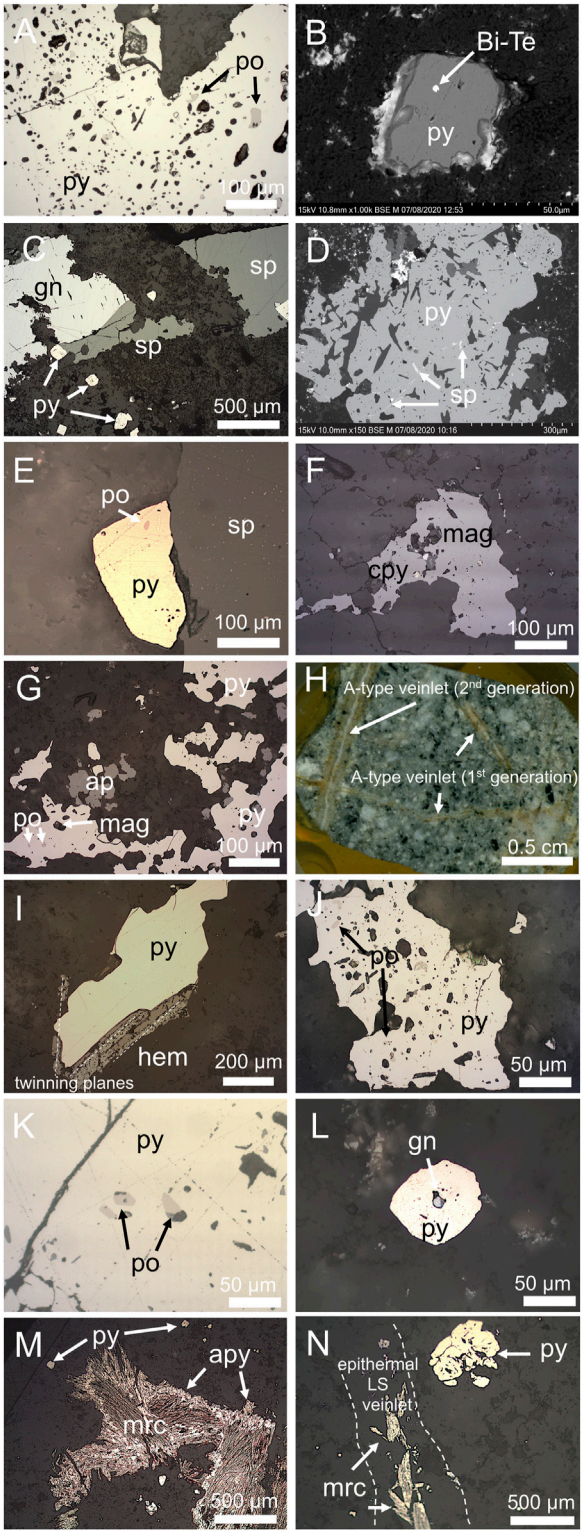

FIGURE 4
Scans, microphotographs, and back-scattered electron images of mineralized samples from the two hydrothermal systems at Kaspakas and Sardes: **(A)** Porous pyrite, featuring pyrrhotite from the Kaspakas sericitic altered sample LEM-1; (*Continued*)

epithermal stage is hosted by sedimentary rocks. The IS epithermal stage at Sardes is characterized by quartz and calcite veins, hosting pyrite and base metal sulfides (e.g., LEM-33). The LS epithermal alteration at Sardes prospect is expressed by hydrothermal quartz veinlets hosted by sedimentary rocks. It is characterized by arsenopyrite as well as marcasite (cf. Section 4.2; LEM-33; Figure 2C) and may be part of the IS epithermal stage of Sardes, which it overprints.

4.2 Ore and gangue mineralogy

The epithermal and porphyry mineralization at Limnos can be subdivided into two types including a 1) host rock and 2) vein-related mineralization, which exhibits a distinct mineralogy between the different prospects and their alteration stages (cf. Section 4.1).

4.2.1 Fakos

Magnetite related to the porphyry stage either occurs in quartz-magnetite veinlets (LM-JB-20), as disseminated patches, or massive accumulations (LM-84, LM-97B, LM-JB-19) in the host rocks of the potassic alteration zone. Minor chalcopyrite and pyrite accompany the quartz-magnetite veinlets. Hematite is a minor constituent along grain boundaries and fractures in the magnetite (Figure 3A). Small inclusions of rutile were rarely observed in pyrite (Figure 3B).

FIGURE 4 (Continued)
(B) BSE image of pyrite featuring an inclusion of an unidentified Bi-Te mineral from sericitic sample LEM-7 (Kaspakas). Note that high contrast snowflake like objects around the pyrite grain are lead dust as a result of polishing on a lead plate; **(C)** euhedral to subhedral pyrite in anhedral galena, sphalerite and the surrounding calcite of epithermal IS sample LEM-19, Kaspakas; **(D)** BSE image of porous pyrite with a small sphalerite vein as well as sphalerite inclusions, LEM-6 epithermal IS Kaspakas LEM-6; **(E)** Microphotograph of pyrite with a pyrrhotite inclusion, next to sphalerite in an epithermal IS vein of LEM-19; **(F)** Chalcopyrite grains in magnetite of LEM-40, Sardes potassic alteration; **(G)** Porphyry potassic altered sample (Sardes) LEM-35 with pyrite and apatite, the anhedral pyrite has pyrrhotite and magnetite inclusions; **(H)** scan of the polished ore section LEM-40 from the Sardes potassic alteration zone. Two generations of A-type veinlets with alteration haloes; **(I)** Pyrite and hematite in vein of LEM-35, Sardes potassic alteration; **(J)** Porous pyrite, featuring pyrrhotite from the propylitic altered sample LEM-51, Sardes; **(K)** reflected light image of pyrrhotite in pyrite (Sardes epithermal IS LEM-33); **(L)** Small pyrite with galena inclusion (LEM-33), Sardes; **(M)** Epithermal IS stage pyrite in close vicinity of low-sulfidation epithermal veinlets with marcasite laths, covered in microscopic arsenopyrite, (LEM-33) Sardes; **(N)** Pyrite from the intermediate sulfidation pyrite next to an epithermal LS vein with marcasite, (LEM-33) Sardes. Mineral abbreviations after Whitney and Evans (2010): Py–pyrite, Apy–arsenopyrite, Mrc–marcasite, Ccp–chalcopyrite, Sp–sphalerite, Gn–galena, Mag–magnetite, Hem–hematite, Tnt-Ttr–tetrahedrite-tennantite, Po–pyrrhotite, Eng–enargite, Mol–molybdenite, Qz–quartz, Ap–Apatite.

Alteration selvages of diopside, epidote, sanidine and minor biotite rarely occur in association with the quartz-magnetite veinlets (LM-JB-20, Supplementary Table S3). Pyrite dominates the sericitic alteration stage at Fakos, where it is accompanied by minor chalcopyrite and accessory molybdenite (Figure 2A). In this assemblage, pyrite occurs in fine quartz veinlets or disseminated within the altered quartz-monzonite (Figure 3C). Epithermal veinlets hosting sphalerite rarely cross-cut the porphyry mineralization of the sericitic alteration (LM-64, Figure 3D).

Pyrite is the most abundant sulfide in the transitional stage (Figure 2A). In the vicinity of the Fakos quartz-monzonite, pyrite occurs disseminated in the altered sandstone together with tourmaline (LM-JB-14), where it commonly hosts pyrrhotite inclusions. Several generations of quartz/tourmaline veinlets have been recorded (Figures 3E,F), which either host pyrite and lack an alteration halo (Figure 3F) or are devoid of pyrite and exhibit an alteration selvage consisting of quartz and sericite (i.e., white mica). At the west coast of the Fakos peninsula, the transitional stage (JB-LM-03) consists of crustiform banded carbonate veins, cross-cutting the sandstone beds (Figure 3G). The carbonate veins are associated with fine-grained iron-oxides, clay, and pyrite, which sometimes also host pyrrhotite inclusions (Figure 3H).

The Fakos HS epithermal stage also hosts abundant pyrite, with minor sphalerite and galena (Figure 2A). Pyrite is extensively brecciated and commonly occurs in silicified veinlets. Some pyrites show porous and dense domains (Figure 3O) and host inclusions of chalcopyrite, galena, and sulfosalts like tennantite and enargite (Figures 3I,J). In addition, anhedral sphalerite occurs interstitial between the pyrite grains and in voids (Figure 3K). The IS epithermal mineralization is associated with quartz-carbonate veinlets consisting of pyrite, sphalerite, galena, and chalcopyrite (Figures 2A, 3L–N). Chalcopyrite inclusions are also common in the sphalerite (Figure 3L), which occurs in veinlets and disseminated in the altered host rock. Sphalerite hosting chalcopyrite inclusions typically shows serrate grain boundaries in contact to the carbonate gangue (Figure 3L), whereas the inclusion-free sphalerite rather exhibits straight grain boundaries (Figure 3D). Chalcopyrite and galena occur as large anhedral grains that often show intergrowth and infill open voids between euhedral quartz and pyrite (Figure 3M). Silver-rich tetrahedrite (based on EPMA observations) occurs as inclusions in galena (c.f. Supplementary Table S2). Bournonite ($PbCuSbS_3$) and tennantite are rare and occur in breccias, where they are intergrown with pyrite and galena (LM-27B, (Figure 3N). Minor amounts of pyrite are disseminated in the altered host rocks in the vicinity of the mineralized veinlets.

4.2.2 Kaspakas

The sericitic alteration in the Kaspakas porphyry is dominated by porous pyrite with minor pyrrhotite

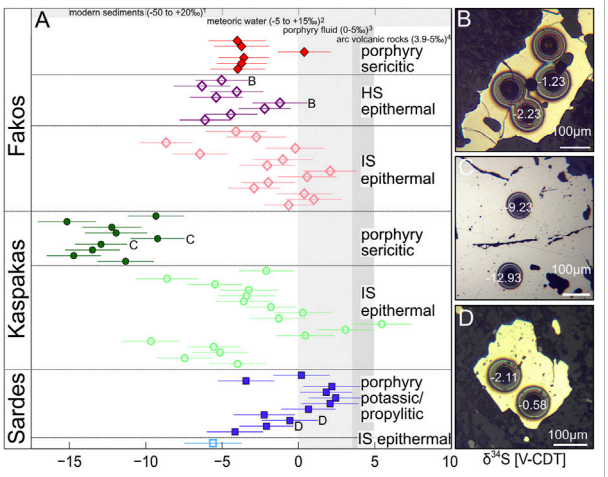

FIGURE 5
(A) *In situ* $\delta^{34}S_{V\text{-}CDT}$ of pyrite from the different hydrothermal systems and related alteration/mineralization stages. Measurements in **(A)** labeled with B, C or D correspond to **(B–D)** showing the $\delta^{34}S$ variations in individual pyrite grains from the three prospects. The data is available in the electronic annex (Supplementary Table S7). The grey boxes in **(A)** represent literature data for the isotopic range S sources ([1]modern sediments (Seal, 2006); [2]meteoric water (Geyh et al., 2000); [3]porphyry fluids (Hutchison et al., 2020); [4]arc volcanic rocks (Falkenberg et al., 2022, and references therein) Modern seawater at ~21‰ is not show in this figure (Rees et al., 1978; Tostevin et al., 2014).

(Figure 4A) and rarely hosts inclusions of an unspecified Bi-Te mineral (Figure 4B). Pyrite either occurs in veinlets (LEM-1, -7) or forms patches in the altered host rock (LEM-3BII). In the IS epithermal stage, carbonate veins with minor gangue quartz (LEM-19 III) contain galena, sphalerite, and minor euhedral pyrite (Figure 4C). Minor tennantite-tetrahedrite was identified as inclusions in vein-related pyrite (LEM-19 III). Inclusions of sphalerite, galena, and pyrrhotite were recorded in disseminated pyrite from the IS epithermal stage (Figures 4D,E).

4.2.3 Sardes

Anhedral and partly porous magnetite with chalcopyrite inclusions occurs in the potassic alteration zone at Sardes (Figure 4F). Minor pyrite with pyrrhotite inclusions is present in patches together with the magnetite (Figure 4G). Pyrite-bearing veinlets (LEM-35) and two generations of quartz-magnetite-chalcopyrite veinlets (LEM-40, LEM-65) were observed in this alteration assemblage (Figure 4H). Hematite may also occur in close relation to pyrite in these veinlets (LEM-35, Figure 4I). The first generation of the quartz-magnetite-chalcopyrite veinlets is dominated by quartz and magnetite with only subordinate chalcopyrite, which is cross-cut by the second generation, where quartz and chalcopyrite are more abundant compared to magnetite. Anhedral to subhedral pyrite in the propylitic alteration zone is disseminated in the host rock and has minor inclusions of pyrrhotite and quartz

(Figure 4J). Pyrite typically exhibits porous as well as dense domains and serrate grain boundaries (Figure 4K).

The IS epithermal stage found at Sardes hosts galena and pyrite that occur disseminated in the host rocks. Pyrite locally hosts small inclusions of pyrrhotite (Figure 4K), galena and carbonate (Figure 4L). The LS epithermal alteration at Sardes is characterized by marcasite that is surrounded by arsenopyrite, and overprints parts of the IS epithermal alteration (Figures 4M,N).

4.3 *In-situ* S isotope composition of pyrite

The *in situ* $\delta^{34}S_{VCDT}$ composition of pyrite varies from −15.2 to 5.4‰ (Figure 5) and significant variations were observed between the different mineralization stages of Limnos (Figure 5A; Supplementary Table S7). At Fakos, the $\delta^{34}S$ composition of pyrite ranges from −4‰ to 0.4‰ in the porphyry sericitic alteration and from −8.7‰ to 2.1‰ in the IS epithermal stage. This is in agreement with previous analyses by Fornadel et al. (2012) showing $\delta^{34}S$ variations of −6.8 to −0.8‰ (n = 5) and −5.3 to −2.2‰ (n = 4) in porphyry and epithermal pyrite from Fakos, respectively. Porphyry pyrite from Fakos shows a relatively constant $\delta^{34}S$ value of about -4‰, with the exception of one outlier at 0.4‰. Variations of up to 1‰ were detected within individual pyrite grains at Fakos (Figure 5B), which is however insignificant regarding the measurement uncertainty of ~1.7‰ in the data acquisition (cf. Section 3.3; Supplementary Table S7). Pyrite from the porphyry sericitic alteration at Kaspakas is light in $\delta^{34}S$, as reflected by $\delta^{34}S$ values as low as −15.2‰. Variations of up to 3.7‰ $\delta^{34}S$, were observed within individual pyrite grains from the sericitic alteration at Kaspakas, which is outside the measurement uncertainty (Figures 5A,C). We note that this isotopic variation may actually be larger than recorded by our measurement, as the 50 µm beam diameter and 90 s ablation time homogenize a large volume of pyrite. The $\delta^{34}S$ values of pyrite from the IS epithermal stage at Kaspakas are generally higher than those of the porphyry stage, but show a large variation from −9.6 to 5.4‰ (Figure 5A). At Sardes, the $\delta^{34}S$ composition of pyrite from potassic (−4.2 to −0.6‰) and propylitic (−3.5 to 2.4‰) alteration in the porphyry stage are higher than in IS epithermal pyrite (−5.6‰). Variations within individual pyrite grains are insignificant with respect to the analytical uncertainty (Figure 5D).

4.4 Trace element chemistry of sulfides

Most pyrite from the investigated prospects has a near pure composition. Arsenic concentrations in pyrite are generally low (<0.5 wt.%, n = 257). The exception is some epithermal pyrite from the IS stage at Fakos (n = 5) and Kaspakas (n = 5), where As is >0.5 wt.% and reaches up to 2.7 wt%. The highest median As contents at Fakos are displayed by pyrite from the transitional stage, whereas those of the porphyry and epithermal stage are characterized by lower median values (Figure 6A). The median As content in IS epithermal pyrite from Kaspakas and Sardes is more than an order of magnitude higher than in pyrite from the porphyry stage (Figure 6A; Table 4). We note that the potassic and propylitic alteration at Sardes were combined, due to the small number of pyrite analysis from the propylitic stage and their comparable chemical composition. Arsenic, Sb, Te, and Au show the same relative distribution in pyrite from the porphyry to epithermal stages at Kaspakas and Sardes (Figures 6B–D). The pyrite from all investigated IS epithermal stages is typically enriched in these elements with respect to their median values. Tellurium and Au however behave differently at Fakos, where the highest median values were observed in the porphyry sericitic pyrite rather than the IS epithermal stage. Irrespective of the mineralization stage, pyrite from Fakos shows the highest median values in Sb, Te, and Au, which contrasts the distribution of As (Figures 6A–D). Selenium is enriched in porphyry compared to epithermal pyrite at Fakos and Kaspakas, whereas the median values at Sardes are comparable. In addition, higher Se contents were observed in HS epithermal compared to IS epithermal pyrite from Fakos (Figure 6E). Cobalt and Ni show higher concentrations in pyrite from the porphyry and transitional stage, than in the epithermal stage at Fakos (Figure 6F; Table 4). Pyrite from the HS epithermal stage of Fakos is depleted in Ni, Co, As, Sb, Te and Au compared to the IS epithermal pyrite of Fakos. Overall, the highest median values of As, Sb, and Au were observed in marcasite from the LS epithermal stage (Table 5). Galena from the IS epithermal stage generally exhibits the highest median Se, Te, Ag, Tl, and Bi contents relative to the other sulfides (Table 5).

Correlations between different trace elements are generally poorly developed in pyrite. However, pyrite from the different alteration stages and prospects can be classified by variable trace element ratios (Figure 7). For example, epithermal pyrite from Fakos shows more variable Co/Ni and As/Co values than pyrite from the related porphyry stage. Pyrite from the transitional stage at Fakos exhibits particularly high As/Co values (>10), that partly overlap with the values of the IS epithermal stage from Fakos and Kaspakas. In contrast to porphyry sericitic pyrite from Fakos, those from Sardes and Kaspakas show a much wider Co/Ni range, which is comparable to the epithermal pyrite from the same prospect (Figures 7A,B). The Sb and Pb contents in pyrite show a tendency towards higher concentrations in IS epithermal pyrite, which partly overlap with the pyrite data from the Vatukoula LS epithermal deposit (Figure 7C; Börner et al., 2021). A similar relation is expressed between Tl and Pb in pyrite from the three prospects on Limnos Island (Figure 7D). The Sb/Pb and Tl/Pb values of pyrite between the different alteration stages from the same location are comparable

10.3389/feart.2022.916107

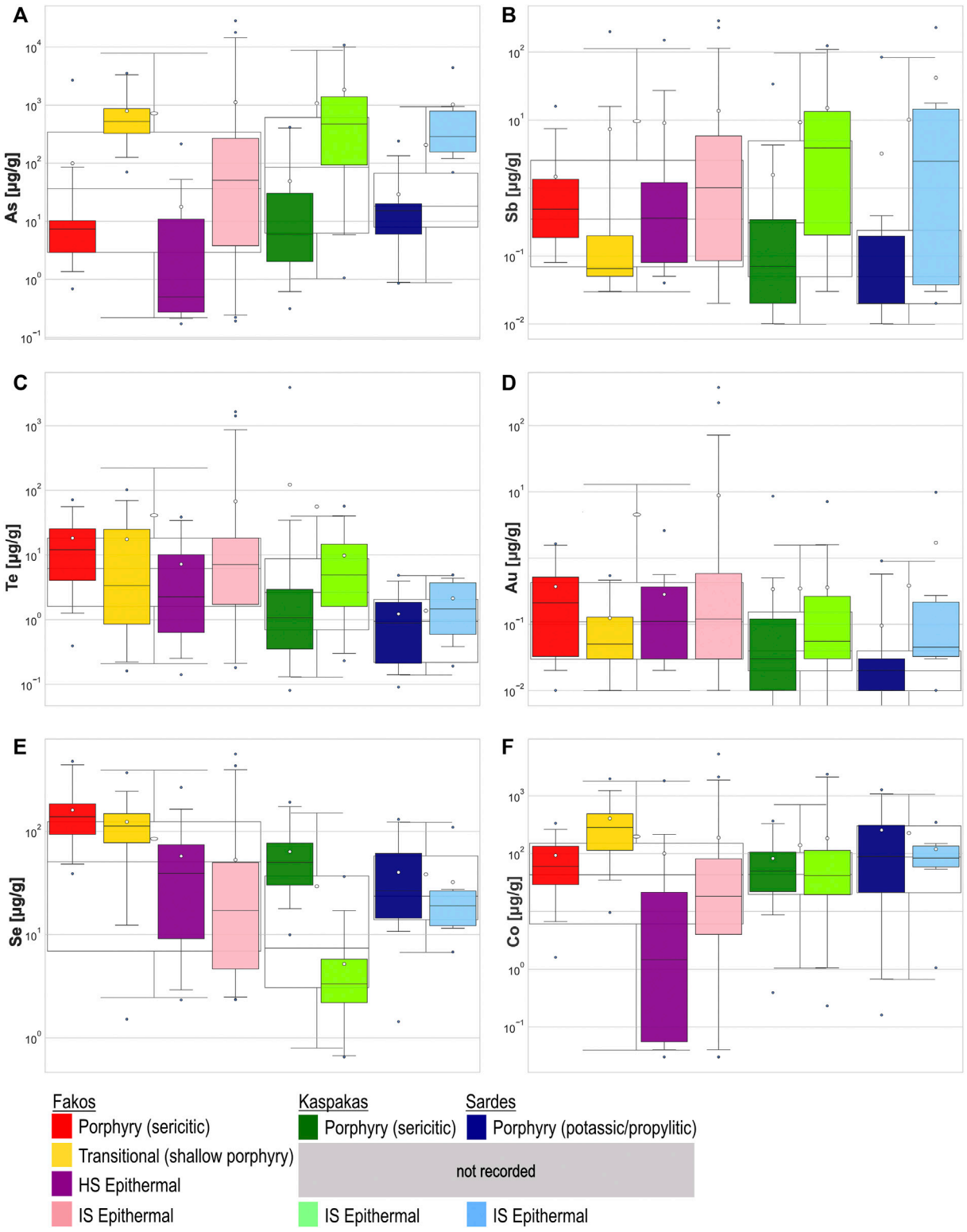

FIGURE 6
Box and whisker plots of trace elements in pyrite. **(A)** As; **(B)** Sb; **(C)** Te; **(D)** Au; **(E)** Se; **(F)** Co, each in µg/g. Note that the presented data includes the detection limits of the individual analyses. The box represents 50% of the data and the whiskers the 2nd and 98th percentile. The horizontal line in the box is the mean value and the cross the median value, which includes the outliers. The large black outlined box in the background summarizes the data of the different prospects irrespective of the related alteration/mineralization stages.

TABLE 4 Summary of pyrite results from LA-ICP-MS analysis.

	Mn (μg/g)	Co (μg/g)	Ni (μg/g)	Cu (μg/g)	Zn (μg/g)	Ga (μg/g)	Ge (μg/g)	As (μg/g)	Se (μg/g)	Ag (μg/g)	Cd (μg/g)	In (μg/g)	Sn (μg/g)	Sb (μg/g)	Te (μg/g)	Au (μg/g)	Tl (μg/g)	Pb (μg/g)	Bi (μg/g)
Fakos porphyry sericitic																			
(n>LOD)/n	n.a.	30/30	30/30	30/30	2/30	n.a.	n.a.	30/30	30/30	22/30	2/30	n.a.	n.a.	28/30	29/30	25/30	13/30	30/30	28/30
Min		1.59	31.46	0.82	<2.56			0.68	38.8	<0.02	<0.09			<0.04	<0.15	<0.014	<0.0067	0.16	<0.006
Max		332	918	1909	143			2663	475	10.6	0.19			15.9	70.9	1.63	0.13	475.2	19.6
SD		86.6	247	349	97.8			484	103	2.92	0.06			3.16	18.6	0.45	0.03	86.1	4.27
MEDIAN		59.33	284.63	5.31	4.27			7.25	138.04	0.30	0.19			0.49	11.99	0.21	0.02	6.41	0.69
Fakos transitional																			
(n>LOD)/n	32/32	32/32	32/32	24/32	5/32	6/32	25/32	32/32	31/32	13/32	5/32	32/32	5/32	14/32	28/32	22/32	6/32	28/32	30/32
Min	14.8	9.50	16.34	<0.16	<0.70	<0.03	<0.49	69.8	<1.51	<0.02	<0.004	0.01	<0.07	<0.03	<0.16	<0.0006	<0.009	<0.02	<0.02
Max	62.7	1960	3594	40.7	4.92	0.61	1.43	3505	368	4.55	0.26	0.02	1.44	197	101	0.54	5.09	536	43.5
SD	17.3	240	210	1.34	1.18	0.06	0.70	541	94.7	0.06	0.14	0.01	0.12	0.16	3.96	0.06	0.02	3.53	0.80
MEDIAN	16.04	282.42	207.20	1.05	1.17	0.05	0.67	516.04	112.16	0.03	0.17	0.01	0.11	0.06	3.34	0.05	0.02	6.79	1.25
Fakos epithermal HS																			
(n>LOD)/n	n.a.	19/23	22/23	23/23	5/23	n.a.	n.a.	14/23	23/23	17/23	4/23	n.a.	n.a.	21/23	20/23	18/23	8/23	22/23	23/23
Min		<0.02	<0.17	2.47	<2.17			<0.17	2.32	<0.02	<0.08			<0.02	<0.11	<0.006	<0.004	<0.03	0.05
Max		1810	5996	5890	71.5			212	265	36.9	0.18			148	38.3	2.58	0.81	3686	146
SD		412	1302	1177	28.9			56.1	65.4	9.63	0.04			32.4	10.9	0.58	0.27	855	32.6
MEDIAN		1.45	20.69	599.41	3.42			0.49	38.99	1.22	0.16			0.36	2.24	0.11	0.01	1.66	8.08
Fakos epithermal IS																			
(n>LOD)/n	52/72	67/72	63/72	72/72	40/72	16/72	20/72	59/72	67/72	62/72	31/72	52/72	7/72	53/72	67/72	55/72	42/72	71/72	53/72
Min	<15.50	<0.03	<0.19	0.15	<0.92	<0.03	<0.36	<0.19	<2.33	<0.01	<0.06	<0.001	<0.06	<0.02	<0.001	<0.004	<0.0002	<0.03	<0.01
Max	4,373.09	5258.16	1820.89	40951.23	2190.55	5.71	1.50	27952.45	559.74	2536.88	29.68	19.82	2.78	286.16	1630.26	373.10	3.89	7818.00	71.30
SD	531.99	657.94	337.24	4,483.62	341.17	0.71	0.24	4,083.16	93.14	325.65	3.67	3.07	0.33	41.93	250.65	46.68	0.44	862.90	8.32
MEDIAN	22.35	18.06	48.81	22.03	3.33	0.06	0.63	50.20	17.05	1.01	0.24	0.01	0.13	1.00	7.07	0.12	0.02	27.84	0.16
Kaspakas porphyry sericitic																			
(n>LOD)/n	24/25	25/25	20/25	3/25	13/25	21/25	22/25	24/25	10/25	1/25	4/25	10/25	13/25	19/25	13/25	14/25	25/25	22/25	24/25
Min	<0.05	<0.01	<0.06	<0.06	<1.06	<0.01	<0.17	<0.15	<0.51	<3.02	<0.002	<2.68	<0.02	<4.82	<2.58	<4.95	<4.52	<0.008	<7.3E-6
Max	612	712	6565	676	50	10.5	3.21	732	191	71.5	0.79	0.41	22.8	33.7	3874	8.53	0.58	5996	423
SD	95.5	133	952	102	14.2	2.07	0.47	152	47.1	14.2	0.37	0.14	7.17	7.36	611	1.76	0.12	982	62.1
MEDIAN	17.85	48.41	21.01	0.92	2.43	0.08	0.66	4.61	60.58	0.02	0.18	0.01	0.12	0.07	1.06	0.04	0.02	6.63	1.02
Kaspakas epithermal IS																			
(n>LOD)/n	47/54	54/54	53/54	54/54	1/54	54/54	54/54	54/54	12/54	53/54	3/54	54/54	38/54	54/54	21/54	40/54	54/54	52/54	47/54
Min	16.2	0.23	2.67	0.55	<1.50	<0.01	<0.1	74.3	<0.37	<0.0002	<0.0007	<8.2 E-5	<0.05	0.17	<0.001	<3.5E-05	<7.6E-5	3.51	0.05
Max	330	2352	323	44	7189	3.69	10.3	10663	7.44	24.4	66.3	2.76	7.58	122	56.6	7.07	0.76	15029	138
SD	57.7	556	62.4	120	2141	0.96	2.02	3239	1.79	4.58	22.9	0.86	2.49	33.5	12.9	1.37	0.16	2722	25.4
MEDIAN	23.32	43.35	48.38	6.48	3.58	0.35	0.89	329.41	4.35	0.15	0.20	0.01	0.15	1.07	3.93	0.04	0.04	119.28	4.14
Sardes porphyry potassic																			
(n>LOD)/n	27/27	27/27	27/27	22/27	9/27	13/27	23/27	27/27	26/27	15/27	4/27	8/27	8/27	14/27	23/27	10/27	9/27	25/27	20/27
Min	15	0.16	0.85	<0.08	<1.23	<0.01	<0.15	0.85	<0.54	<1.8E-06	<0.08	<1.3E-6	<0.06	<0.008	<9.1E-6	<2.4E-07	<0.003	<0.01	<8.9E-7
Max	233	1264	752	441	2714	3.87	29.2	238.17	130.3	2.72	36.2	1.01	700	83.4	4.82	0.90	0.27	11168	13.8
SD	49.9	371	161	94.8	900	1.02	5.93	50	35.2	0.86	17.9	0.37	247	22.2	1.24	0.30	0.09	2229	3.24
MEDIAN	23.42	88.34	19.06	0.34	2.91	0.05	0.71	15.01	26.52	0.03	0.20	0.01	0.11	0.02	0.88	0.02	0.01	3.21	0.43
Sardes epithermal IS																			
(n>LOD)/n	21/21	21/21	21/21	17/21	5/21	8/21	16/21	21/21	21/21	13/21	5/21	1/21	3/21	15/21	20/21	13/21	10/21	20/21	18/21
Min	17.52	1.05	25.61	0.17	1.18	0.02	0.62	68.93	6.76	0.01	0.12	0.00	0.09	0.02	0.19	0.01	0.01	0.13	0.01
Max	24.08	344.76	3983.33	127.78	4.42	0.13	0.96	4,376.64	109.28	15.80	0.20	0.02	0.30	227.21	4.89	9.77	7.15	102.78	1.34
SD	2.73	120.66	1349.52	50.94	1.22	0.04	0.11	1677.66	38.57	6.40	0.03	0.00	0.07	91.17	2.02	3.96	2.91	40.07	0.61
MEDIAN	18.34	83.08	1210.46	4.40	3.81	0.06	0.86	283.96	18.95	0.04	0.18	0.01	0.18	2.46	1.46	0.05	0.03	5.63	0.35

Abbreviations: *n*, number of samples; LOD, limit of detection; SD, standard deviation.

10.3389/feart.2022.916107

TABLE 5 Summary of results from LA-ICP-MS analysis of minor ore mineral.

	Mn (μg/g)	Fe (μg/g)	Co (μg/g)	Ni (μg/g)	Cu (μg/g)	Zn (μg/g)	Ga (μg/g)	Ge (μg/g)	As (μg/g)	Se (μg/g)	Ag (μg/g)	Cd (μg/g)	In (μg/g)	Sn (μg/g)	Sb (μg/g)	Te (μg/g)	Au (μg/g)	Tl (μg/g)	Bi (μg/g)
Chalcopyrite (Sardes porphyry: *n* = 3)																			
(n > LOD)/n	3/3	n.a.	3/3	3/3	n.a.	3/3	3/3	3/3	3/3	3/3	3/3	3/3	3/3	3/3	3/3	2/3	2/3	3/3	3/3
Min	20.1		0.43	1.34		149	0.62	1.98	2.54	81.9	3.01	4.22	9.31	0.81	0.14	0.00	0.00	0.05	0.13
Max	21.8		1.06	1.77		336	0.84	3.31	6.01	123	4.30	13.5	11.9	1.05	0.29	4.13	0.13	0.08	0.46
SD	0.99		0.35	0.22		104	0.11	0.70	1.75	22	0.70	5.08	1.31	0.13	0.08	2.12	0.06	0.02	0.16
MEDIAN	21.7		0.48	1.55		163	0.74	3.06	4.73	90	4.14	12.5	10.9	0.82	0.17	1.24	0.08	0.06	0.30
Chalcopyrite (Fakos epithermal IS: *n* = 16)																			
(n>LOD)/n	5/16	n.a.	16/16.	1/16	n.a.	16/16	3/16	1/16	4/16	7/16	16/16	13/16	5/16	2/16	13/16	3/16	2/16	3/16	3/16
Min	<1.14		0.07	<0.55		69.7	<0.17	<1.61	<0.60	<2.49	1.39	<0.31	<0.02	<0.33	<0.10	<0.44	<5.43	<0.02	<0.02
Max	13		0.26	0.71		2207	2.45	2.70	5.78	70.9	186	18.2	63.6	2.25	33.8	1.29	0.41	0.1	0.14
SD	0.55		0.06	n.a.		564	1.26	n.a.	1.53	23.8	57	6.12	33.5	0.99	9.08	0.22	0.25	0.04	0.05
MEDIAN	12.7		0.15	0.92		192	0.35	2.62	1.11	6.82	70.6	2.83	5.03	0.44	0.49	0.88	0.07	0.03	0.03
Galena (Fakos epithermal IS: *n* = 23; Kaspakas epithermal IS: *n* = 1)																			
(n>LOD)/n	10/24	4/24	2/24	1/24	12/24	2/24	n.a.	n.a.	5/24	24/24	24/24	24/24	11/24	2/24	24/24	24/24	20/24	24/24	24/24
Min	0.33	<7.9	<0.02	<0.15	<0.27	<1.65			<0.17	20.5	133	30.7	<0.0003	<0.12	129	7.29	0.03	16.8	2.87
Max	39.1	88.6	0.20	0.93	605.1	659			15.4	2208	1615	276	0.09	0.41	1533	607	1.25	121	1634
SD	11.7	27.6	0.10	n.a.	173	319			6.60	551	392	53.36	0.03	0.13	328	118	0.33	32.4	353
MEDIAN	1.45	13.8	0.06	0.43	0.54	2.85			0.50	320	399	46.9	0.02	0.20	398	86.9	0.18	24	121
Marcasite (Sardes epithermal LS: *n* = 10)																			
(n>LOD)/n	10/10	n.a.	10/10	10/10	10/10	5/10	8/10	6/10	10/10	10/10	10/10	5/10	7/10	9/10	10/10	10/10	10/10	10/10	10/10
Min	17.5		5.85	54.4	99.4	<0.03	<0.5	<0.56	29997	7.87	20.3	<0.0004	<0.14	<0.03	657	7.23	3.33	4.64	0.41
Max	1232		16.6	173	8030	1761	74.7	10.2	4899137	92.4	69.6	12.6	20.6	45.9	80373	4588	32.4	51.6	6.07
SD	382		2.95	38.7	2468	784	26.2	3.81	1519545	27.4	16.3	5.46	7.77	14.9	24908	1441	10.8	14.1	1.60
MEDIAN	21.2		10.4	106	202	4.99	0.43	0.98	60400	20	50	0.32	0.03	0.48	1250	26.7	13.5	8.52	1.23
Sphalerite (Fakos epithermal HS: *n* = 10; Fakos epithermal IS: *n* = 41; Kaspakas epithermal IS: *n* = 15)																			
(n>LOD)/n	53/66	66/66	65/66	43/66	66/66	n.a.	53/66	13/66	21/66	30/66	66/66	66/66	53/66	49/66	44/66	13/66	29/66	28/66	27/66
Min	<0.1	258	0.03	<0.09	25.9		<0.02	<0.18	<0.18	<0.59	0.18	2067	<1.7E-5	<0.06	<0.012	<0.001	<3.5E-05	<4.8E-5	<1.8E-6
Max	6265	13208	90.1	3.58	18120		170	11.2	168	7.77	234	5898	43.6	20.8	2048	6.68	1.21	2.41	11.7
SD	1709	2711	29.7	0.8	3563		33.7	3.52	36.8	1.75	28.8	996	6.32	5.05	308	1.79	0.22	0.63	2.25
MEDIAN	2961	5388	5.37	0.79	1906		5.49	0.42	0.46	2.32	2.80	3580	2.05	1.62	0.18	0.19	0.03	0.01	0.01

Abbreviations: *n*, number of samples; LOD, limit of detection; SD, standard deviation.

10.3389/feart.2022.916107

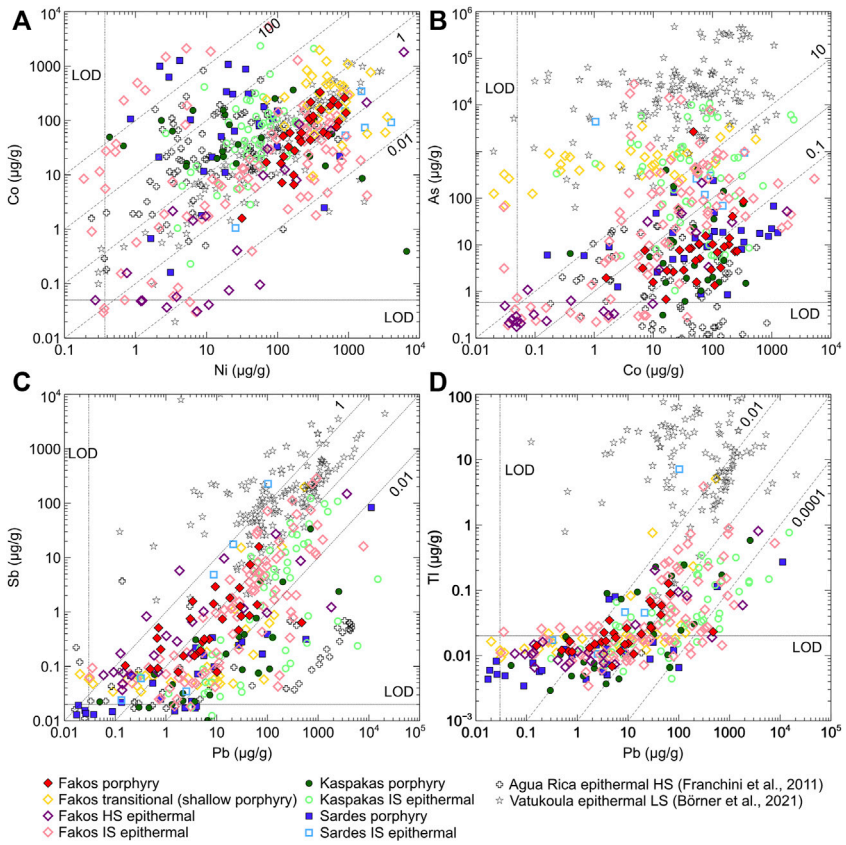

FIGURE 7
Trace element correlation diagrams of pyrite from the different hydrothermal systems and related alteration/mineralization stages: **(A)** Co-Ni, **(B)** As-Co, **(C)** Sb-Pb, **(D)** Tl-Pb. The data from Agua Rica, Argentina, is from Franchini et al. (2015) and the data from Vatukoula, Fiji, is from Börner et al. (2021). The black dashed line represents the ratio of the respective elements in the diagram. Dotted lines represent the highest limit of detection.

(Figures 7C,D), and a high Sb/Pb and Tl/Pb end member is defined by pyrite from Vatukoula.

5 Discussion

5.1 Paragenetic sequence of alteration and mineralization

5.1.1 Fakos

Cross-cutting relationships and alteration assemblages suggest multiple hydrothermal pulses during the porphyry stage at Fakos (Figures 3, 4; Fornadel et al., 2012). Early magnetite ± hematite ± chalcopyrite ± pyrite veinlets, with potassic alteration halos are the first stage of the porphyry mineralization at Fakos. In this assemblage, chalcopyrite, and pyrite typically infill cavities in the magnetite (Figure 3A), and therefore precipitated contemporaneously or following the magnetite (Figure 2A). The sericitic pyrite is adjoined by minor molybdenite, presumably also from the sericitic stage (Figure 3D). Fluid inclusions measured by Fornadel et al. (2012) suggest entrapment depths <1200m, with outliers as deep as 2.5 km. Pyrite from the sericitic alteration stage hosts inclusions of rutile, these may be remnant from the earlier potassic stage (Figure 3B; Rabbia et al., 2009) or have formed due to the breakdown of primary TiO_2-bearing mineral phases (Schirra and Laurent, 2021). Both scenarios are consistent with a sericitic overprint of the potassic alteration zone. An overprint is also documented in the literature (Fornadel et al., 2012; Voudouris et al., 2019a). The irregular boundaries of the veins in the potassic alteration (Figure 3C) are a typical textural feature of high-temperature ductile deformation at lithostatic pressure conditions (Lindsay et al., 1995), which classifies them as A-type veins (Sillitoe, 2010). Mineralization temperatures of the A-type veins associated with a potassic alteration assemblage are suggested to be related to temperatures >500°C (Monecke et al., 2018). This also agrees with fluid inclusion data of quartz from genetically related samples at Fakos, indicating temperatures of up to 780°C at salinities of up to 85.8 wt.% NaCl equivalent (Fornadel et al., 2012). However, the dominant

pyrite mineralization in the residual A-type veins (Figure 3C) indicates that they have been overprinted by the sericitic alteration stage.

The sandstone-hosted tourmaline-quartz to calcite dominated veins (Figure 3E) of the transitional stage (or shallow porphyry; c.f. 4.1) at Fakos comprise characteristics of both, porphyry and epithermal alteration, as reflected by the occurrence of molybdenite- and sphalerite-bearing veins (Fornadel et al., 2012), and as also supported by the pyrite chemistry (cf. Section 5.3). The pyrite (±pyrrhotite) mineralization that is associated with the tourmaline veins (Figures 2A, 3E,H) cross-cuts an earlier barren quartz vein (Figure 3F). The evolution from tourmaline- to carbonate-dominated veins (Figures 3E,G) in the transitional zone towards the western coast of the Fakos peninsula (Tables 1–3; Figure 1C) may be related to the increasing distance to the magmatic center and the feeder zone of the porphyry fluids. Well-documented E-W trending fault zones in the center of the Fakos peninsula controlled the fluid flow and the formation of the transitional stage in the vicinity of the quartz monzonite (Figure 1C). As such, these fractures may have acted as pathways for the magma-derived fluids from deeper crystallizing levels into the overlying sediments. Here, they most likely interacted with increasing proportions of meteoric waters or seawater towards the western coast, as reflected by the increasing abundance of carbonate and the occurrence of galena, which is indicative for epithermal conditions at lower fluid temperatures (<300°C; Reed and Palandri, 2006). This agrees with the kaolinite-nacrite alteration together with alunite along the western coast of the Fakos peninsula (Figure 1C; Tables 1, 2; and Supplementary Table S3), which indicates low temperature alteration (150–200°C) by acidic fluids. This either suggests that the fluids were partly derived from a magmatic source (Hedenquist et al., 2017; Fornadel et al., 2012; Fulignati, 2020) or that vapor-rich fluids were formed by boiling and condensed into seawater and/or meteoric water fluids in a steam-heated environment leading to the acid alteration (Naden et al., 2005; Keith et al., 2020; Schaarschmidt et al., 2021b; Nestmeyer et al., 2021).

A late epithermal stage is documented by the occurrence of E-type veins that host minor sphalerite (Figure 3D) together with enargite (Figure 3I). This reflects HS epithermal conditions and therefore is attributed to the HS epithermal stage, described by Fornadel et al. (2012) (Figure 2A; Einaudi et al., 2003). We propose that the porous and dense domains in pyrite from the HS epithermal stage (Figures 3J,O) may have formed during boiling and non-boiling conditions, respectively (Román et al., 2019). Vapor-rich fluid inclusions in quartz from the epithermal environment at Fakos have been proposed to possibly be related to boiling in this stage by Fornadel et al. (2012) further corroborate this. Boiling and accompanying vapor release can also explains the brecciation of the pyrite due to small scale boiling-related hydraulic fracturing (Figure 3K; Román et al., 2019). Because sphalerite lacks signs of brecciation and occurs along cracks in the brecciated pyrite (Figure 3K) we infer that sphalerite precipitated after the boiling, which also indicates changes in the temperature-pressure regime (Monecke et al., 2018; Hurtig et al., 2021). Later stage IS epithermal conditions are recorded by tennantite-tetrahedrite inclusions in sphalerite, pyrite, and quartz in the E-type veins (Figures 2A, 3L) that overprint the sericitic and chloritic alteration (Supplementary Table S2). Pyrite forms early in this assemblage, as galena, tetrahedrite, and bournonite occur between fragments of brecciated pyrite (Figure 3N). As such, the mineralization at Fakos shows features of a telescoped porphyry-epithermal system. This is indicated by an early potassic alteration stage, overprinted by sericitic alteration, which was followed by a late-stage epithermal mineralization and overprint (Figure 2A). The common occurrence of pyrite together with rare pyrrhotite (Figure 2A), as observed in the transitional stage (Figure 3H), indicates that the fluid conditions were likely in the range of the pyrite-pyrrhotite stability line (Einaudi et al., 2003).

5.1.2 Kaspakas

Similar to Fakos transitional and IS epithermal stages, the mineralization of the sericitic alteration and the IS epithermal stage at Kaspakas likely also evolved along the pyrite-pyrrhotite stability line, as indicated by pyrrhotite inclusions in pyrite (Figures 4A,E). The porous nature of the pyrite in the sericitic alteration (Figure 4A) may further indicate that boiling accompanied the fluid evolution (Román et al., 2019). The IS epithermal stage is indicated by the formation of sphalerite, galena and the occurrence of tennantite-tetrahedrite (Supplementary Table S2; Einaudi et al., 2003; Voudouris et al., 2019b). Hence, the fluid evolution from the porphyry, to IS epithermal stage at Kaspakas likely included combination of fluid cooling and boiling and mixing (cf. Sections 5.2, 5.3).

5.1.3 Sardes

Two vein types in the potassic alteration at Sardes can be subdivided, including earlier A-type veinlets (1st generation) comprising quartz and magnetite with minor chalcopyrite, which are crosscut by later stage A-type veinlets (2nd generation), where chalcopyrite is more abundant than magnetite which only occurs in minor amounts (Figure 4H). The development from an earlier magnetite- towards a later sulfide-dominated mineralization is likely related to cooling and/or decreasing fO_2 and increasing fS_2 conditions with proceeding fluid evolution (Einaudi et al., 2003). Locally, textural evidence suggests the formation of pyrite after hematite at Sardes (Figure 4I), which is in contrast to the pyrite-hematite relation at Fakos. The pyrrhotite inclusions occur only in dense domains of pyrite, which we attribute to non-boiling conditions (Román et al., 2019) in the propylitic alteration. This suggest a co-precipitation of these two minerals along the pyrrhotite-pyrite stability line (Figure 4K; Einaudi et al., 2003).

TABLE 6 Overview of key characteristics and processes at the investigated hydrothermal stages of Fakos, Kaspakas and Sardes.

Location and alteration stage	Key ore minerals and fluid inclusion data[a]	$\delta^{34}S$ in pyrite	Trace elements in pyrite	Key fluid processes
Fakos (sericitic)	Pyrite, molybdenite, rutile	Stable inter- and intra- grain composition; min: −4‰, max: 0.4‰, median: −3.7‰	↑Se, Co, Te, Au ↓As	Fluid- host-rock interaction, overprint of potassic alteration, cooling
Fakos (transitional)	Pyrite—pyrrhotite, molybdenite, sphalerite, tourmaline, calcite, clays	Not analyzed, section to thin for analysis	↑As, Te, Se, Co ↓Sb, Au	Boiling, mixing, cooling
Fakos (HS epithermal)	Enargite	min: −6.3‰, max: −1.2‰, median: −4.7‰	↓As, Te, Se, Co	Boiling, cooling, mixing
Fakos (IS epithermal)	(193°–262°c, 1.4–4.7 wt.% NaCl equiv.)	High variability; min: −8.7‰, max: 2‰, median: −1.5‰	↑As, Sb, Te, Au ↓Se, Co	Boiling, mixing, cooling
Kaspakas (sericitic)	Pyrite—pyrrhotite	Very low; strong intragrain variability; min: −15.1‰, max: −9.2‰, median: −12.2‰	↑Se ↓As, Sb, Te, Au	Boiling (separated pockets), cooling
Kaspakas (IS epithermal)	Pyrite—pyrrhotite	Highest variation; min: −9.7‰, max: 5.4‰, median: −3.3‰	↑As, Sb, Te, Au ↓Se	Boiling, mixing (vapor condensation), cooling
Sardes (potassic + propylitic)	Pyrite—pyrrhotite	min: −4.2‰, max: 2.4‰, median: 0.2‰	↑As, Sb, Te, Au ↓Se, Co	Phase separation, mixing (propylitic)
Sardes (IS epithermal)	Pyrite—pyrrhotite, marcasite-arsenopyrite	−5.6‰	↑As, Sb, Te, Au ↓Se	Boiling, mixing (vapor condensation), cooling

[a]Fornadel et al.(2012).

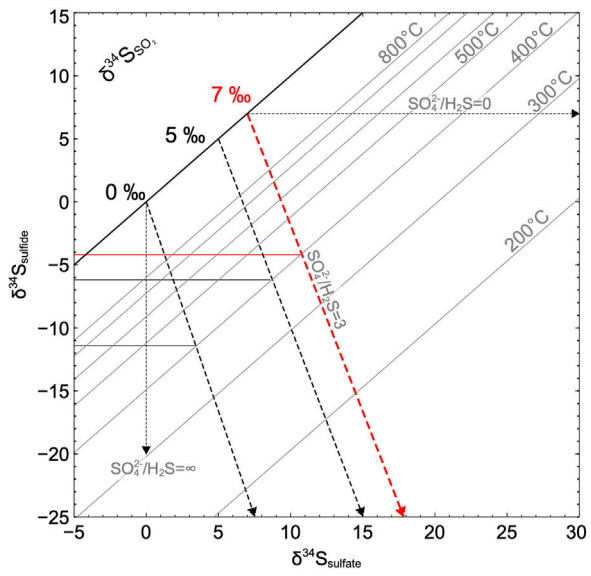

FIGURE 8
Model for the $\delta^{34}S$ evolution of sulfides and sulfates, derived from a hydrothermal fluid primarily consisting of magmatic SO_2. The isotopic fractionation is related to temperature and the disproportionation of the hydrothermal fluid. Model adapted after Hutchison et al. (2020).

The IS epithermal stage commonly hosts disseminated pyrite with pyrrhotite or galena inclusions (Figures 2C, 4K,L). Hence, the hydrothermal fluid of the IS epithermal stage was also in the range of the pyrite-pyrrhotite stability line in both, the porphyry and the epithermal environment, as also proposed for Fakos and Kaspakas. The LS epithermal mineral assemblage of Sardes is indicated by arsenopyrite that postdates marcasite (Figures 4M,N). Marcasite stability indicates further fluid cooling to temperatures <240°C (Murowchick and Barnes, 1986), where pyrite is absent (Figure 2C). We note that the LS mineral assemblage of Sardes overprints an IS assemblage. The LS epithermal event may therefore represent fluctuating conditions in the IS epithermal dominated stage at Sardes. Low sulfidation epithermal systems are usually found in the more distal parts of hydrothermal systems (Einaudi et al., 2003; Camprubí and Albinson, 2007), therefore we cannot rule out the influence of a later or neighboring system completely.

We conclude that for each of the prospects, an early-stage porphyry mineralization at the ductile-brittle (potassic: Fakos, Sardes) and lithostatic-hydrostatic (sericitic: Fakos, Kaspakas) transition is preserved. The IS epithermal stage at Kaspakas and Sardes evolved along the pyrite-pyrrhotite stability line (Figures 2B,C; Table 6). At Fakos and Kaspakas a combination of boiling, cooling and mixing between magmatic and meteoric fluids likely formed telescoped porphyry-epithermal environment (cf. Sections 5.2, 5.3; Table 6). For Sardes, the relation between porphyry and IS-LS epithermal are less clear, suggesting a temporal difference or that the epithermal overprint belongs to an adjacent system.

5.2 Insights into sulfur sources and phase separation through $\delta^{34}S$

Sulfur isotopes are commonly used in hydrothermal systems to constrain the contribution of S from different sources in the

crust (e.g., igneous vs sedimentary rocks) and from magmatic or meteoric fluids (including seawater). In addition, mixing between fluids of different origin changes the isotopic composition and processes like phase separation lead to S isotope fraction, which is typically preserved by the sulfides that form from these fluids (McKibben and Eldridge, 1990; Rye, 2005; Seal, 2006; McDermott et al., 2015; Hutchison et al., 2020). Disproportionation of SO_2 is a common process during ascent and cooling of magma-derived fluids, where ^{32}S and ^{34}S fractionate between H_2S and SO_4^{2-}, respectively (Ohmoto and Rye, 1979; Eldridge et al., 2021), as shown by Eq. 3:

$$4SO_2 + 4H_2O \Leftrightarrow H_2S + 3HSO_4^- + 3H^+ \quad (3)$$

According to Kouzmanov and Pokrovski (2012), 99% of the initial SO_2 will have disproportionated after cooling to 400 °C, which is consistent with the fluid temperatures at the transition from the potassic to sericitic alteration (350–400°C; Sillitoe, 2010). However, this can only be achieved by concomitant pH buffering in the ascending fluids (Kouzmanov and Pokrovski, 2012). For example, an earlier formed potassic alteration assemblage, as known from telescoped porphyry systems, such as those on Limnos Island (cf. Section 5.1; Voudouris, 2006; Fornadel et al., 2012). Magmatic fluids typically have a primary $\delta^{34}S_{SO2}$ composition in the range of 0‰–5‰ (Figure 8; Hutchison et al., 2020). Porphyry sulfides that form from the H_2S portion of these fluids following the SO_2 disproportionation cluster around −1‰ in $\delta^{34}S$ and vary from −10 to 9‰, whereas epithermal sulfides cluster around −2‰ and show a range from −23 to 8‰ (Hutchison et al., 2020).

The $\delta^{34}S$ composition of pyrite from the Fakos porphyry sericitic stage shows little variation (Figure 5A) and mostly cluster around a value of -4‰. Therefore they are isotopically lighter with respect to the average value of porphyry sulfides (-1‰) associated with calc-alkaline magmas and the $\delta^{34}S_{SO2}$ range (0‰–5‰) of the parental magmatic fluids (Hutchison et al., 2020). This either indicates isotope disequilibrium conditions between the fluid and the pyrite during precipitation or that the $\delta^{34}S_{H2S}$ of the magma-derived fluid following SO_2 disproportionation was modified by other processes such boiling (McKibben and Eldridge, 1990). Additionally, it is possible, that the $\delta^{34}S_{SO2}$ composition of the parental magmatic fluid was not in the range of 0‰–5‰, as proposed by Hutchinson et al. (2020). A contribution from (meta-) sediment melts to the magmatic S budget could lead such a difference in isotopic composition of the magmatic fluid. The very narrow range in $\delta^{34}S$ in the porphyry pyrite from Fakos, except one outlier at 0.4‰, and the relatively small $\delta^{34}S$ range of ~1‰ within single pyrite crystals (Figure 5B), which is within the analytical uncertainty (cf. Section 3.3), correlates with rather small variations in trace element ratios like Co/Ni (Figure 7; cf. Section 5.3). This suggests negligible changes in fluid conditions leading to S isotope fractionation. Therefore, the more likely scenario to produce the measured isotopic values, is a slow and steady pyrite precipitation rate in S isotope equilibrium with the magma-derived fluid and without significant changes in fluid composition. This would exclude the processes of phase separation or fluid mixing, which we would expect to have been preserved by a more variable $\delta^{34}S$ range (Schaarschmidt et al., 2021b). Modelled $\delta^{34}S$ values of sulfides that precipitated from a parental magmatic fluid released from a calc-alkaline magma ($\delta^{34}S_{SO2}$ of 0–5‰; Hutchison et al., 2020), following SO_2 disproportionation and assuming a SO_4^{2-}/H_2S ratio of 3 according to Eq. 3, should vary between −6 and −11‰ at temperatures of 400°C (Figure 8), which is typical for sericitic alteration zones (Sillitoe, 2010). While assumed temperatures of 500 °C would result in an initial $\delta^{34}S_{SO2}$ of 5‰ after Hutchison et al. (2020), these temperatures would rather refer to a potassic than a sericitic alteration. Hence, the $\delta^{34}S$ composition of pyrite from the sericitic alteration at Fakos cannot be explained by SO_2 disproportionation of a magmatic fluid with a $\delta^{34}S_{SO2}$ value between 0 and 5‰, alone (Figure 5). Instead, we propose a reverse modelling approach, based on the $\delta^{34}S$ composition of the porphyry pyrite from Fakos (about −4‰) and a precipitation temperature of 400 °C, that the initial magmatic fluids were isotopically heavier at ~7‰ $\delta^{34}S_{SO2}$ with an uncertainty of ±1‰, considering the fluid-sulfide S isotope fraction at equilibrium conditions (Figure 8; McDermott et al., 2015). Why the initial $\delta^{34}S_{SO2}$ composition of the magma-derived fluids from Limnos Island are isotopically heavier than those from other porphyry systems remains elusive. A contribution of S from (meta-) sediments, which are present in this area, could have influenced the $\delta^{34}S_{SO2}$ of the related magmatic fluids. This, however, requires further investigation, which is out of scope of this study. We conclude that the $\delta^{34}S$ composition of pyrite from the sericitic alteration zone at Fakos reflects the H_2S portion of the parental magmatic fluid following SO_2 disproportionation and cooling from >700 to ~400°C (Figures 8, 9). The process that produced the $\delta^{34}S$ composition of the outlier at 0.4‰ remains unclear (Figure 5). The outlier at 0.4‰ may be related to following hydrothermal events that overprinted the sericitic alteration, or a remnant of the previous potassic alteration (cf. Section 5.1). Evidence for affiliation with the later-stage epithermal pyrites is provided by similar $\delta^{34}S$ values (Figure 5A).

The influx of seawater ($\delta^{34}S_{SO4}$ ~ 21‰; Rees et al., 1978; Tostevin et al., 2014) or meteoric water ($\delta^{34}S_{SO4}$ ~ −5–10‰; Geyh et al., 2000) is a common process under hydrostatic conditions, which can result in significant $\delta^{34}S$ variations in magmatic-hydrothermal fluids and upon sulfate reduction in the $\delta^{34}S$ composition of the sulfide precipitates relative to the proposed $\delta^{34}S$ composition of the parental magmatic fluid (Figure 8; McDermott et al., 2015; Hutchison et al., 2020). Deeply circulated meteoric fluids and/or seawater that underwent thermal equilibration with the host rocks are capable of transporting S from e.g. (meta-) sediments into the hydrothermal system. The $\delta^{34}S$ in modern sediments may vary

10.3389/feart.2022.916107

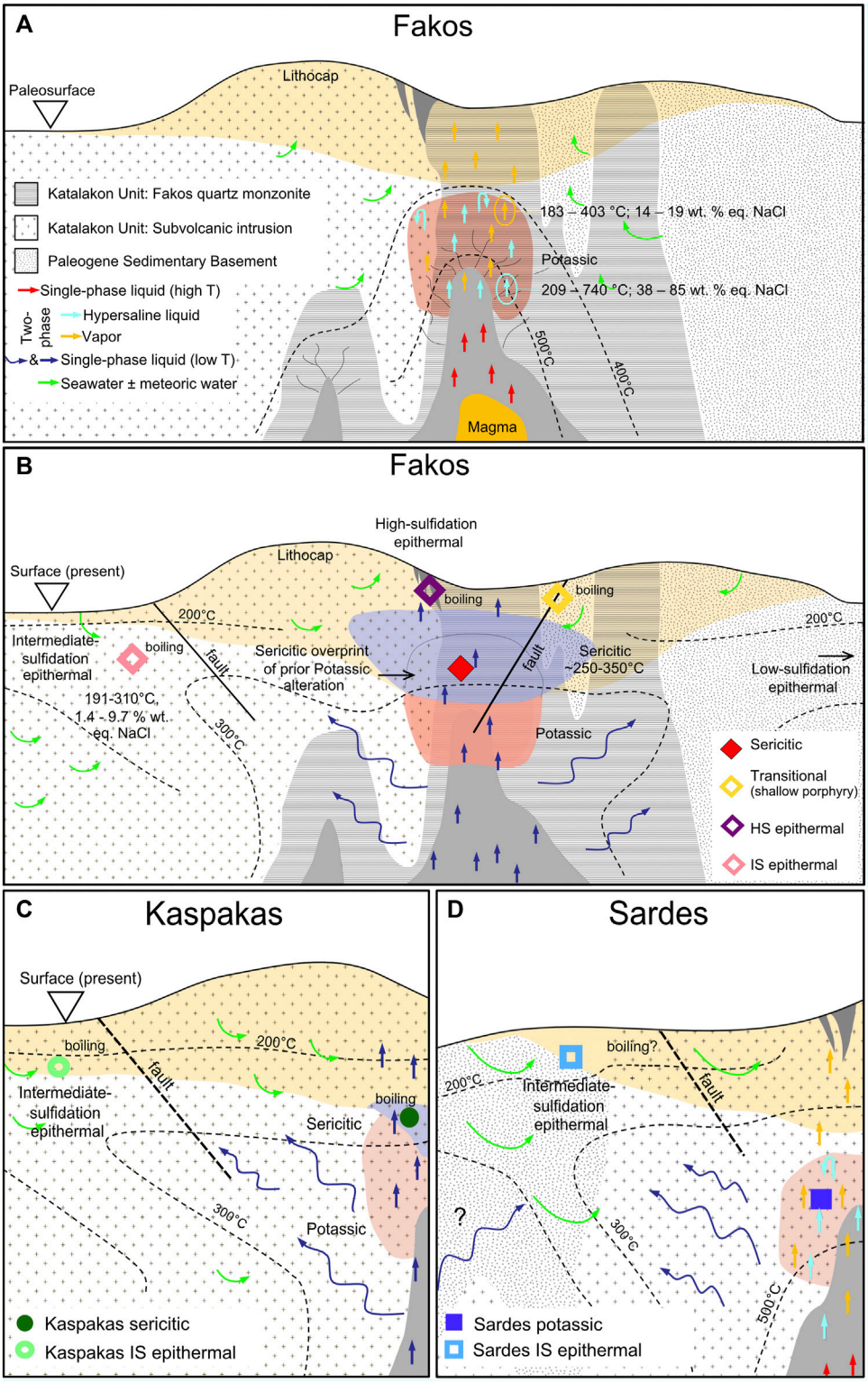

FIGURE 9
Schematic model for the porphyry-epithermal evolution of the three distinct hydrothermal systems: Fakos **(A,B)**, Kaspakas **(C)** and Sardes **(D)**. Modified after Sillitoe (2010). Details about the different processes as presented in the text (cf. Sections 5.2, 5.3).

significantly between −50‰ and 20‰ as reported by Seal (2006). For this reason, in systems which allow an influx of seawater and/or meteoric waters (hydrostatic pressure conditions), these additional factors may significantly influence the isotopic S signature. Fluid boiling is an important process that may lead to strong local S isotope fractionation resulting in a significant ^{34}S decrease in the H_2S portion of the fluid due to H_2S oxidation to SO_4^{2-} (McKibben and Eldridge, 1990), as shown by Eq. 4:

$$H_2S_{(aq)} + 4H_2O \rightleftharpoons SO_{4(aq)}^{-2} + 2H^+ + 4H_{2(g)} \quad (4)$$

When pockets of fluid get isolated, for example, through tectonic faulting or hydrothermal fracturing, large proportions of the fluid may undergo this coupled boiling-oxidation process. In a closed system without influx of "fresh" H_2S that may dilute the $\delta^{34}S_{H2S}$ signature to higher values towards the original fluid prior to boiling, this may result in $\delta^{34}S$ values of hydrothermal sulfides that are significantly lower than the respective $\delta^{34}S_{H2S}$ composition of the fluid prior to boiling (Ohmoto and Lasaga, 1982; McKibben and Eldridge, 1990). Such a process may be reflected by the extremely low $\delta^{34}S$ values (below -10‰) of porphyry pyrite from the sericitic alteration at Kaspakas (Figure 5). This is supported by significant $\delta^{34}S$ variations that were observed within single pyrite grains (>3‰, Figure 5B), which indicates abrupt changes in fluid conditions possibly by fluid boiling causing S isotope fractionation (Ohmoto and Lasaga, 1982; McKibben and Eldridge, 1990; Schaarschmidt et al., 2021b). Hence, hydrothermal fracturing related to boiling and tectonic faulting may have isolated fluid pockets in the sericitic alteration at Kaspakas (Figure 9). This is in contrast to the processes proposed for the sericitic alteration at Fakos, where evidence for such boiling-related S isotope fractionation is lacking. We note that we deem the influence of sedimentary or metasedimentary sources of the $\delta^{34}S$ on the isotopic signature of Kaspakas Sericitic stage pyrite unfit to explain the large intragrain variability of $\delta^{34}S$. In addition, while limited influence from partial melting of sediments and (meta-) sediments may be present in the $\delta^{34}S$ signature of the primary magmatic fluid, extreme low values (<−10‰) would require vast amounts of (meta-) sedimentary contribution. Because no further geochemical evidence for this contribution has been recorded, we dismiss this as the primary source of the extreme $\delta^{34}S$ variations in Kaspakas sericitic stage.

At the Fakos epithermal system, fluid inclusion temperatures (193°–262°C) and salinities (1.4–4.7 wt.% NaCl equiv.) are consistent with fluid boiling (Fornadel et al., 2012). The $\delta^{34}S$ signatures in pyrite from the HS and IS epithermal stage overlap with the $\delta^{34}S$ signatures in the proposed parental magmatic fluid, but also show a much wider variation than the latter (Figure 5). We propose, in combination with the fluid inclusion data by Fornadel et al. (2012), the pyrite textures (c.f. 5.1.1), and the trace element data (c.f. 5.3), that these $\delta^{34}S$ variations are caused by boiling of a fluid that was at least partly derived from a magmatic source (Figure 9). The lack of such extremely negative values as observed in porphyry pyrite from Kaspakas may be due to open system boiling, as part of a more continuous fluid flux towards the surface. However, with increasing influence form seawater and/or meteoric water, (meta-) sedimentary derived S cannot be dismissed as an additional possible influence on the sulfur isotopy in pyrite (Table 6; Figure 9). The higher $\delta^{34}S$ values of some pyrites relative to those of the porphyry stage serve as a record of this (Figure 5). This is in agreement with the conclusion of Fornadel et al. (2012) that $\delta^{34}S$ values of 10.5‰ in barite from the IS epithermal stage suggest mixing of magmatic fluids and seawater. The variability in the $\delta^{34}S$ data of pyrite from the HS epithermal stage is less pronounced and more similar to the porphyry pyrites. This may be caused by the proximity of the HS mineralization to the magmatic feeder zone, allowing less influence of seawater and/or meteoric water (Figure 9; Hedenquist and Lowenstern, 1994). The lower $\delta^{34}S$ values in IS epithermal pyrite from Kaspakas relative to the proposed parental magmatic fluid signature (Figure 5) are likely multicausal: 1) Fluid boiling in an open system with concomitant oxidation, 2) Mixing with S which was transported through other fluids (e.g., deeply circulated meteoric and/or seawater fluids that underwent thermal equilibration with host rock).

Since no extreme negative values as displayed by the related porphyry pyrites at Kaspakas were observed, we dismiss a strong boiling of separated fluid pockets for the Fakos pyrites. In addition, the higher $\delta^{34}S$ values (>4‰) suggest a contribution of S transported by deeply circulated seawater and/or meteoric water, mixing with the magma-derived fluids or possibly the condensation of boiling-derived vapors into the latter (cf. Section 5.3, Table 6; Figure 9).

The negative $\delta^{34}S$ values in porphyry pyrite from Sardes that overlap with the pyrite from sericitic alteration at Fakos (~4‰) are consistent with a magmatic fluid source. By contrast, the heavier $\delta^{34}S$ values (>4‰) at Sardes are likely related to an increased contribution of S that was transported through seawater and/or meteoric water, which is more common in propylitic altered rocks (cf. Section 5.3, Figure 9). For the IS epithermal pyrite from Sardes low $\delta^{34}S$ values may be explained by a mixture of the processes mentioned in this section. However, the LS event within the IS epithermal stage does point towards lower temperatures and in conjunction with the low $\delta^{34}S$ values towards a stronger influence of seawater and/or meteoric water as well as possibility for boiling.

We conclude that the $\delta^{34}S$ signature of pyrite provides insights into S sourcing, mixing of fluids, and isotope fractionation during SO_2 disproportionation and fluid boiling, which affected the mineralization of the investigated prospects to variable degrees mostly controlled by the geological and tectonic conditions (Table 6; Figure 9).

5.3 Trace element signatures in pyrite for phase separation and fluid-rock interaction

High temperature pyrite (>350°C) from porphyry systems is commonly depleted in most trace elements, except for Ni, Co, and Se, relative to epithermal pyrite that forms at lower temperatures (<350°C) (Franchini et al., 2015; Sykora et al., 2018; Zhang et al., 2018; Rivas-Romero et al., 2021). Both Co and Ni are mainly transported as Cl^- complexes in hydrothermal fluids, and are therefore sensitive to changes in fluid salinity and pH (Liu et al., 2011; Brugger et al., 2016). However, Co seems to be slightly more sensitive to fluid salinity and temperature than Ni, indicating that Ni may stay in solution at lower temperatures and salinities relative to Co (Liu et al., 2011, 2012). The Co/Ni values of pyrite from Limnos Island, exhibit a higher variability than other porphyry and epithermal systems like Agua Rica, Argentina (Franchini et al., 2015), and Vatukoula, Fiji (Figure 7A; Börner et al., 2021). This indicates that the porphyry-epithermal fluids and their precipitates were affected by drastic changes in fluid temperature and salinity, which may be related to phase separating processes (Román et al., 2019; Klose et al., 2021). However, the small Co/Ni variations (0.1-1) in porphyry sericitic pyrite from Fakos (Figure 7B) rather point towards more stable fluid conditions than in the other porphyry prospects. This indicates that pyrite precipitation was not controlled by boiling at Fakos sericitic stage. The stable conditions are in agreement with the small variety in the $\delta^{34}S$ values of these pyrites (Figure 5), consistent with precipitation under non-boiling conditions (Figure 9). By contrast, the Co/Ni values of pyrite from all other mineralization stages of the different prospects on Limnos is highly variable (Figure 7A). This indicates strong temperature and/or salinity variations possibly related to phase separation (Figure 9), which is also supported the $\delta^{34}S$ data of these systems (cf. Section 5.2, Figure 5).

The ratio of volatile (e.g., As, Sb) to non-volatile (e.g., Co, Pb) elements may vary between low Cl vapor- and high Cl liquid-rich fluids that formed by boiling and may be preserved by the ratios of these elements (e.g., As/Co) in the precipitated pyrite (Román et al., 2019; Falkenberg et al., 2021; Klose et al., 2021). Hence, pyrite with As/Co ratios exceeding those of the Fakos porphyry sericitic pyrite (>0.1-1), precipitated from a vapor-rich fluid (Figure 7). This is supported by the existence of quartz-hosted vapor-rich (≤5% liquid) fluid inclusions with salinities of 1–10 wt.% NaCl equivalent and homogenization temperatures <300°C that are common in the E-type veins of the Fakos system (Fornadel et al., 2012). Hence, fluid boiling seems to be a likely process in the investigated epithermal stages as well as Kaspakas porphyry sericitic stage (Figure 9). For the Sardes porphyry potassic-propylitic stage, no clear evidence for boiling or vapor- hypersaline liquid separation was recorded, however, the observed trace-element signatures rather overlap with those of Kaspakas porphyry sericitic (boiling) than those of Fakos porphyry sericitic (non-boiling). Nonetheless, an increased influence of seawater and/or meteoric water must be assumed in the propylitic stage of Sardes. No effect of phase separation is documented by the Sb/Pb and Tl/Pb values of pyrite, as indicated by similar ratios between pyrite from the sericitic stage at Fakos, where evidence for boiling separation is lacking, and the other investigated systems. This may be due to a superimposed temperature control on the solubility of Sb, Tl, and Pb, which tend to be enriched in pyrite that forms at lower temperatures (<300°C; Maslennikov et al., 2009; Falkenberg et al., 2021). This agrees with tendency of the epithermal pyrite of this study to higher Sb, Tl, and Pb values than the porphyry pyrites (Figure 7C,D). The Sb, Tl, and Pb values for the epithermal pyrites of this study partly overlap with the data from the Vatukoula LS epithermal deposit, where fluid temperatures were in the range of 160–300°C with documented boiling (Ahmad et al., 1987).

We propose the following model for the Au and Te distribution in porphyry-epithermal pyrite from Limnos Island. At Fakos, the sericitic alteration that overprints the earlier potassic alteration (Figure 9, Table 6 cf. Section 5.1) is mainly controlled by magma-derived fluids that lack evidence for phase separation. As a consequence, the fluids forming the sericitic alteration may have been buffered by the alteration minerals of the potassic alteration (e.g., sanidine or biotite), leading to higher pH values than if they would be buffered in fresh rock (Kouzmanov and Pokrovski, 2012). Importantly, the solubility of Au and Te increases with increasing fluid pH (Kouzmanov and Pokrovski, 2012; Grundler et al., 2013; Smith et al., 2017), whereas decreasing fO_2 may cause the Te precipitation (Grundler et al., 2013; Gao et al., 2017; Keith et al., 2020) and the deposition of Au is commonly related to decreasing H_2S conditions (Heinrich, 2005; Grundler et al., 2013). During fluid-ascent, fO_2 and H_2S may vary significantly as a result of host rock oxidation and sulfidation. We therefore propose that the interaction of the fluids with the host rocks led to a decrease in fO_2 and H_2S (Figure 9), causing a contemporaneous precipitation of Te and Au in the Fakos porphyry sericitic stage (Gao et al., 2017; Keith et al., 2020). Tellurium is depleted in the later stage and shallower epithermal environment in pyrite of the HS relative to the IS stage (Figure 6C). Hence, parts of the Te likely precipitated at greater depth or the later stage fluids were generally characterized by lower Te contents. The higher Te and Au contents in pyrite from the IS epithermal relative to the HS epithermal stage may indicate that limited proportions of these metals may have also been contributed by metaliferous deelpy circulated seawater and/or meteoric water derived fluids, as also indicated by the $\delta^{34}S$ values (c.f. 5.2, Table 6). In the epithermal stage, vapor-rich fluids that formed during phase separation, then precipitated into seawater and/or meteoric water derived fluids, inducing the sulfide precipitation (Figure 9).

In contrast to Fakos, Te (and Au) are enriched in pyrite from the IS epithermal relative to porphyry stage at Kaspakas and

Sardes. We propose that phase separation in the deeper porphyry environment led to the release of Te-rich vapors that ascended towards the surface. Some of the Au likely precipitated in the porphyry environment due to H_2S loss to the vapor phase during this process (Heinrich, 2005). Hence the Au enrichment in the IS epithermal compared to the porphyry pyrite suggests another Au source, likely related to deelpy circulated metalliferous seawater and/or meteoric water, as suggested for Fakos, into which the Te-rich vapor condensed. Similarly, deelpy circulated seawater and/or meteoric water derived fluids likely also contributed base metals like Zn and Pb to the IS epithermal stage at Kaspakas and Sardes, as reflected by the occurrence of sphalerite and galena (Figures 2A–C, 4). We therefore propose that the porphyry-epithermal mineralization in the investigated hydrothermal systems is the result of a combination of phase separation, vapor condensation/mixing and cooling (Table 6, Figure 9).

5.4 Summary and conclusion

The studied samples from the different prospects on Limnos Island that relate to various alteration stages represent snapshots in time and space during the evolution of the respective (telescoped) porphyry-epithermal system. The mineralization related to the Fakos quartz-monzonite is the most extensive in terms of spatial and temporal evolution compared to the Kaspakas and Sardes prospects, as indicated by cross-cutting relationships and alteration overprints. The mineralization in the early potassic alteration at Fakos was mainly controlled by vapor-hypersaline liquid separation, which was followed by a later sericitic overprint. The sericitic alteration that overprints the earlier potassic alteration is related to a single-phase magma-derived fluid at temperatures <400°C. Evidence for boiling or vapor- hypersaline liquid separation is lacking during the sericitic stage at Fakos, as reflected by relatively constant $\delta^{34}S$ (about -4‰) and Co/Ni (0.1-1) values of pyrite. The fluids that caused the sericitic overprint were likely buffered to higher pH due to interaction with the minerals of the potassic alteration which it overprinted. This led to decreasing fO_2 and fS_2, caused by host rock oxidation and sulfidation, which induced the Te and Au precipitation and resulted in the enrichment of these elements in pyrite from the sericitic relative to the epithermal stage at Fakos. At all other investigated prospects and stages, the highly variable $\delta^{34}S$ values (−15.2 to 5.4‰) of pyrite relative to pyrite purely from magma-derived fluid (about −4‰ $\delta^{34}S_{H2S}$) suggest that phase separation and/or fluid mixing strongly influenced the mineralization processes. We propose that during the formation of the sericitic stage at Kaspakas, boiling fluid pockets were isolated from a continuous influx of magma-derived H_2S through hydrothermal fracturing. Strongly negative $\delta^{34}S$ values (−10–15‰) and up to 3.7‰ intragrain variations are the result. By contrast, the epithermal pyrites of the three prospects do not show such negative $\delta^{34}S$ compositions and rather plot between a $\delta^{34}S$ of 4‰ and the proposed endmember pyrite at Kaspakas. This may reflect open system boiling, but could also be influenced by sedimentary derived S that was transported into the systems through seawater and/or meteoric water fluids. Highly variable Co/Ni and high As/Co ratios in pyrite underline the importance of phase separation as a mineralization process. As such, the Te (and Au) enrichment in epithermal relative to porphyry pyrite at Kaspakas and Sardes is suggested to be related to the condensation of Te-rich vapors into metalliferous (Au-bearing) seawater and/or meteoric water derived fluids. Higher $\delta^{34}S$ values in pyrite from the epithermal stages relative to those from the porphyry stages indicate a contribution of isotopically heavier S transported into the system by seawater and/or meteoric water derived fluids. In addition, positive correlations of Sb and Tl with Pb and increasing content of these elements together with decreasing Se in pyrite from the porphyry to the epithermal stage are indicative for continuous cooling to temperatures <300°C during fluid ascent. We conclude that the combination of $\delta^{34}S$ and trace element *in-situ* micro-analysis in pyrite provide important insights into the spatial and temporal evolution of porphyry-epithermal systems. This includes the contribution of fluids from different sources including magmatic as well as seawater and/or meteoric water derived fluids alongside hydrothermal processes like fluid-rock interaction, phase separation and cooling.

Data availability statement

The original contributions presented in the study are included in the article/Supplementary Material, further inquiries can be directed to the corresponding author.

Author contributions

JB and PV conducted the field work. MKu performed *in-situ* δ34S work and data reduction. FS conducted μXRF mappings. LA-ICP-MS and EPMA work were carried under the supervision of JB, MKe, and FB. Trace element LA-ICP-MS data reduction was carried out by FB. FB drafted the manuscript, considering the previous MSc thesis by JB. MKu and FS wrote the respective methods sections of the manuscript. MKe conceptualized the study and received the funding. All authors contributed to manuscript revision, read, and approved the submitted version.

Funding

This study was funded by the German Research Foundation (DFG) grant (KE 2395/1-1), Tellurium in natural and synthetic pyrite: Ore-formation and economic implication.

Acknowledgments

We thank Dr. Brätz for her assistance during LA-ICP-MS analysis and Dr. Krumm for his aid with XRD analysis. Further we thank four reviewers and the Editor, RM for their contributions, which significantly improved the quality of this article.

Conflict of interest

The authors declare that the research was conducted in the absence of any commercial or financial relationships that could be construed as a potential conflict of interest.

Publisher's note

All claims expressed in this article are solely those of the authors and do not necessarily represent those of their affiliated organizations, or those of the publisher, the editors and the reviewers. Any product that may be evaluated in this article, or claim that may be made by its manufacturer, is not guaranteed or endorsed by the publisher.

Supplementary material

The Supplementary Material for this article can be found online at: https://www.frontiersin.org/articles/10.3389/feart.2022.916107/full#supplementary-material

References

Ahmad, M., Solomon, M., and Walshe, J. (1987). Mineralogical and geochemical studies of the Emperor gold telluride deposit, Fiji. *Econ. Geol.* 82 (2), 345–370. doi:10.2113/gsecongeo.82.2.345

Barton, P .B., Bethke, P .M., and Roedder, E. (1977). Environment of ore deposition in the Creede mining district, San Juan Mountains, Colorado; Part III, Progress toward interpretation of the chemistry of the ore-forming fluid for the OH Vein. *Econ. Geol.* 72 (1), 1–24. doi:10.2113/gsecongeo.72.1.1

Blundy, J., Mavrogenes, J., Tattitch, B., Sparks, S., and Gilmer, A. (2015). Generation of porphyry copper deposits by gas–brine reaction in volcanic arcs. *Nat. Geosci.* 8 (3), 235–240. doi:10.1038/ngeo2351

Bonev, N., and Beccaletto, L. (2007). From syn-to post-orogenic tertiary extension in the north aegean region: constraints on the kinematics in the eastern rhodope–thrace, Bulgaria–Greece and the biga peninsula, NW Turkey. *Geol. Soc. Lond. Spec. Publ.* 291 (1), 113–142. doi:10.1144/sp291.6

Börner, F., Keith, M., Smith, D .J., Barry, T .L., Neumann, T., and Klemd, R. (2021). Fingerprinting fluid evolution by trace elements in epithermal pyrite, Vatukoula Au-Te deposit, Fiji. *Ore Geol. Rev.* 137, 104314. doi:10.1016/j.oregeorev.2021.104314

Brugger, J., Liu, W., Etschmann, B., Mei, Y., Sherman, D .M., and Testemale, D. (2016). A review of the coordination chemistry of hydrothermal systems, or do coordination changes make ore deposits? *Chem. Geol.* 447, 219–253. doi:10.1016/j.chemgeo.2016.10.021

Camprubí, A., and Albinson, T. (2007). Epithermal deposits in Mexico-update of current knowledge, and an empirical reclassification. *Geol. Soc. Am. Special Pap.* 422, 377–415. doi:10.1130/2007.2422(14)

Caracciolo, L., Critelli, S., Innocenti, F., Kolios, N., and Manetti, P. (2011). Unravelling provenance from eocene–oligocene sandstones of the thrace basin, north-east Greece. *Sedimentology* 58 (7), 1988–2011. doi:10.1111/j.1365-3091.2011.01248.x

Cheng, Z .G., Zhang, Z .C., Chai, F .M., Hou, T., Santosh, M., Turesebekov, M., et al. (2018). Carboniferous porphyry Cu-Au deposits in the almalyk orefield, Uzbekistan: the sarycheku and kalmakyr examples. *Int. Geol. Rev.* 60, 1–20. doi:10.1080/00206814.2017.1309996

Cooke, D .R., and McPhail, D. C. (2001). Epithermal Au-Ag-Te mineralization, acupan, baguio district, Philippines: numerical simulations of mineral deposition. *Econ. Geol.* 96 (1), 109–131. doi:10.2113/96.1.109

Crowe, D., and Vaughan, R. (1996). Characterization and use of isotopically homogeneous standards for *in situ* laser microprobe analysis of 34S/32 S ratios. *Am. Mineralogist* 81 (1-2), 187–193. doi:10.2138/am-1996-1-223

De Boorder, H., Spakman, W., White, S., and Wortel, M. (1998). Late Cenozoic mineralization, orogenic collapse and slab detachment in the European Alpine Belt. *Earth Planet. Sci. Lett.* 164 (3-4), 569–575. doi:10.1016/s0012-821x(98)00247-7

Deditius, A .P., Utsunomiya, S., Reich, M., Kesler, S .E., Ewing, R .C., Hough, R., et al. (2011). Trace metal nanoparticles in pyrite. *Ore Geol. Rev.* 42 (1), 32–46. doi:10.1016/j.oregeorev.2011.03.003

Doebelin, N., and Kleeberg, R. (2015). Profex: a graphical user interface for the Rietveld refinement program BGMN. *J. Appl. Crystallogr.* 48 (5), 1573–1580. doi:10.1107/s1600576715014685

Drummond, S. E., and Ohmoto, H. (1985). Chemical evolution and mineral deposition in boiling hydrothermal systems. *Econ. Geol.* 80, 126–147. doi:10.2113/gsecongeo.80.1.126

Einaudi, M .T., Hedenquist, J .W., and Inan, E .E. (2003). Sulfidation state of fluids in active and extinct hydrothermal systems. *Soc. Econ. Geol. Geochem. Soc. Special Publ.* 10, 285–313. doi:10.5382/SP.10.15

Eldridge, D .L., Kamyshny, A., Jr, and Farquhar, J. (2021). Theoretical estimates of equilibrium sulfur isotope effects among aqueous polysulfur and associated compounds with applications to authigenic pyrite formation and hydrothermal disproportionation reactions. *Geochimica Cosmochimica Acta* 310, 281–319. doi:10.1016/j.gca.2021.05.051

Falkenberg, J .J., Keith, M., Haase, K .M., Bach, W., Klemd, R., Strauss, H., et al. (2021). Effects of fluid boiling on Au and volatile element enrichment in submarine arc-related hydrothermal systems. *Geochimica Cosmochimica Acta* 307, 105–132. doi:10.1016/j.gca.2021.05.047

Falkenberg, J .J., Keith, M., Haase, K .M., Sporer, C., Bach, W., Klemd, R., et al. (2022). Spatial variations in magmatic volatile influx and fluid boiling in the submarine hydrothermal systems of niuatahi caldera, Tonga rear arc. *Geochem. Geophys. Geosyst.* 23 (4), e2021GC010259. doi:10.1029/2021gc010259

Flude, S., Haschke, M., and Storey, M. (2017). Application of benchtop micro-XRF to geological materials. *Mineral. Mag.* 81 (4), 923–948. doi:10.1180/minmag.2016.080.150

Fornadel, A .P., Voudouris, P .C., Spry, P .G., and Melfos, V. (2012). Mineralogical, stable isotope, and fluid inclusion studies of spatially related porphyry Cu and epithermal Au-Te mineralization, Fakos Peninsula, Limnos Island, Greece. *Mineral. Petrol.* 105 (1), 85–111. doi:10.1007/s00710-012-0196-8

Fortier, S .M., Nassar, N .T., Lederer, G .W., Brainard, J., Gambogi, J., and McCullough, E .A. (2018). Draft critical mineral list—Summary of methodology and background information—U.S. Geological survey technical input document in response to secretarial order No. 3359. *Open-File Rep.* 15. 1. Reston, VA. doi:10.3133/ofr20181021

Fournier, R .O. (1999). Hydrothermal processes related to movement of fluid from plastic into brittle rock in the magmatic-epithermal environment. *Econ. Geol.* 94 (8), 1193–1211. doi:10.2113/gsecongeo.94.8.1193

Franchini, M., McFarlane, C., Maydagán, L., Reich, M., Lentz, D .R., Meinert, L., et al. (2015). Trace metals in pyrite and marcasite from the Agua Rica porphyry-high sulfidation epithermal deposit, Catamarca, Argentina: Textural features and metal zoning at the porphyry to epithermal transition. *Ore Geol. Rev.* 66, 366–387. doi:10.1016/j.oregeorev.2014.10.022

Fulignati, P. (2020). Clay minerals in hydrothermal systems. *Minerals* 10 (10), 919.

Fytikas, M., Giuliani, O., Innocenti, F., Manetti, P., Mazzuoli, R., Peccerillo, A., et al. (1980). Neogene volcanism of the northern and central Aegean region. *Ann. Geol. Des. Pays Hell.* 30. 106–129.

Fytikas, M., Innocenti, F., Manetti, P., Peccerillo, A., Mazzuoli, R., and Villari, L. (1984). Tertiary to Quaternary evolution of volcanism in the Aegean region. *Geol. Soc. Lond. Spec. Publ.* 17 (1), 687–699. doi:10.1144/gsl.sp.1984.017.01.55

Gao, S., Xu, H., Li, S., Santosh, M., Zhang, D., Yang, L., et al. (2017). Hydrothermal alteration and ore-forming fluids associated with gold-tellurium

mineralization in the Dongping gold deposit, China. *Ore Geol. Rev.* 80, 166–184. doi:10.1016/j.oregeorev.2016.06.023

Geyh, M., D´Amore, F., Darling, G., Paces, T., Pang, Z., and Šilar, J. (2000). "Groundwater saturated and unsaturated zone," in *Environmental isotopes in the hydrological cycle—principles and applications. Technical documents in hydrology—International Atomic Energy Agency and United Nations Educational, Scientific and Cultural Organization* 4, 39.

Gläser, L., Grosche, A., Voudouris, P .C., and Haase, K .M. (2022). The high-K calc-alkaline to shoshonitic volcanism of Limnos, Greece: implications for the geodynamic evolution of the northern aegean. *Contrib. Mineral. Petrol.* 177 (8), 73–20. doi:10.1007/s00410-022-01940-7

Gloeckler, M., Sankin, I., and Zhao, Z. (2013). CdTe solar cells at the threshold to 20% efficiency. *IEEE J. Photovolt.* 3 (4), 1389–1393. doi:10.1109/jphotov.2013.2278661

González-Jiménez, J .M., Piña, R., Kerestedjian, T .N., Gervilla, F., Borrajo, I., Pablo, J .F.-d., et al. (2021). Mechanisms for PdAu enrichment in porphyry-epithermal ores of the Elatsite deposit, Bulgaria. *J. Geochem. Explor.* 220, 106664. doi:10.1016/j.gexplo.2020.106664

Grundler, P .V., Brugger, J., Etschmann, B .E., Helm, L., Liu, W., Spry, P .G., et al. (2013). Speciation of aqueous tellurium (IV) in hydrothermal solutions and vapors, and the role of oxidized tellurium species in Te transport and gold deposition. *Geochimica Cosmochimica Acta* 120, 298–325. doi:10.1016/j.gca.2013.06.009

Hedenquist, J. W., and Lowenstern, J. B. (1994). The role of magmas in the formation of hydrothermal ore deposits. *Nature* 370. 519.

Hedenquist, J .W., and Richards, J .P. (1998). The influence of geochemical techniques on the development of genetic models for porphyry copper deposits. *Rev. Econ. Geol.* 10. 235–256. doi:10.5382/Rev.10.10

Hedenquist, J .W., Arribas, A., and Aoiki, M. (2017). Zonation of sulfate and sulfide minerals and isotopic composition in the far southeast porphyry and lepanto epithermal Cu–Au deposits, Philippines. *Resour. Geol.* 67, 174–196. doi:10.1111/rge.12127

Heinrich, C .A. (2005). The physical and chemical evolution of low-salinity magmatic fluids at the porphyry to epithermal transition: a thermodynamic study. *Min. Depos.* 39 (8), 864–889. doi:10.1007/s00126-004-0461-9

Holwell, D .A., Fiorentini, M., McDonald, I., Lu, Y., Giuliani, A., Smith, D .J., et al. (2019). A metasomatized lithospheric mantle control on the metallogenic signature of post-subduction magmatism. *Nat. Commun.* 10 (1), 3511–3610. doi:10.1038/s41467-019-11065-4

Hurtig, N .C., Migdisov, A .A., and Williams-Jones, A .E. (2021). Are vapor-like fluids viable ore fluids for Cu-Au-Mo porphyry ore formation? *Econ. Geol.* 116 (7), 1599–1624. doi:10.5382/econgeo.4835

Hutchison, W., Finch, A .A., and Boyce, A .J. (2020). The sulfur isotope evolution of magmatic- hydrothermal fluids: insights into ore-forming processes. *Geochimica Cosmochimica Acta* 288, 176–198. doi:10.1016/j.gca.2020.07.042

Innocenti, F., Manetti, P., Mazzuoli, R., Pertusati, P., Fytikas, M., and Kolios, N. (1994). The geology and geodynamic significance of the island of Limnos, North Aegean sea, Greece. *njgpm.* 11. 661–691. doi:10.1127/njgpm/1994/1994/661

Innocenti, F., Mazzuoli, R., and Manetti, P. (2008). "Geological map (scale 1: 50,000) of Limnos island (Greece): Explanatory notes," in *Geological map (scale 1: 50,000) of Limnos island (Greece)* (Europe: IGME), 1000–1011.

Jensen, E .P., and Barton, M .D. (2000). Gold deposits related to alkaline magmatism. *Rev. Econ. Geol.* 13, 279. Gold in 2000. doi:10.5382/Rev.13.08

Jolivet, L., and Brun, J.-P. (2010). Cenozoic geodynamic evolution of the Aegean. *Int. J. Earth Sci.* 99 (1), 109–138. doi:10.1007/s00531-008-0366-4

Kamvisis, I.-N .G. (2019). Lamprophyric rock locations in Greece. *Mineralogia* 50 (1-4), 13–33. doi:10.2478/mipo-2019-0002

Keith, M., Smith, D .J., Doyle, K., Holwell, D .A., Jenkin, G .R .T., Barry, T .L., et al. (2020). Pyrite chemistry: A new window into Au-Te ore-forming processes in alkaline epithermal districts, Cripple Creek, Colorado. *Geochimica Cosmochimica Acta* 274, 172–191. doi:10.1016/j.gca.2020.01.056

Kelley, K .D., and Spry, P .G. (2016). Critical elements in alkaline igneous rock-related epi- thermal gold deposits. *Rev. Econ. Geol.* 16, 195–216. doi:10.1130/abs/2016AM-280787

Kilias, A., and Mountrakis, D. (1998). Tertiary extension of the Rhodope massif associated with granite emplacement (Northern Greece). *Acta Vulcanol.* 10, 331–338.

Klose, L., Keith, M., Hafermaas, D., Kleint, C., Bach, W., Diehl, A., et al. (2021). Trace element and isotope systematics in vent fluids and sulphides from maka volcano, north eastern lau spreading centre: Insights into three-component fluid mixing. *Front. Earth Sci. (Lausanne).* 9. 1–26. doi:10.3389/feart.2021.776925

Kokh, M .A., Assayag, N., Mounic, S., Cartigny, P., Gurenko, A., and Pokrovski, G.S. (2020). Multiple sulfur isotope fractionation in hydrothermal systems in the presence of radical ions and molecular sulfur. *Geochimica Cosmochimica Acta* 285, 100–128. doi:10.1016/j.gca.2020.06.016

Kouzmanov, K., and Pokrovski, G. S. (2012). Hydrothermal controls on metal distribution in porphyry Cu (-Mo-Au) systems. *Special Publ. Soc. Econ. Geol.* 16, 573–618. doi:10.5382/SP.16.22

Kusakabe, M., Komoda, Y., Takano, B., and Abiko, T. (2000). Sulfur isotopic effects in the disproportionation reaction of sulfur dioxide in hydrothermal fluids: implications for the δ34S variations of dissolved bisulfate and elemental sulfur from active crater lakes. *J. Volcanol. Geotherm. Res.* 97 (1-4), 287–307. doi:10.1016/s0377-0273(99)00161-4

Kusebauch, C., Gleeson, S., and Oelze, M. (2019). Coupled partitioning of Au and as into pyrite controls formation of giant Au deposits. *Sci. Adv.* 5, eaav5891. doi:10.1126/sciadv.aav5891

Landtwing, M. R., Pettke, T., Halter, W. E., Heinrich, C. A., Redmond, P. B., Einaudi, M. T., et al. (2005). Copper deposition during quartz dissolution by cooling magmatic–hydrothermal fluids: The Bingham porphyry. *Earth Planet. Sci. Lett.* 235 (1–2), 229–243.

Lee, C.-T .A., Luffi, P., Chin, E .J., Bouchet, R., Dasgupta, R., Morton, D .M., et al. (2012). Copper systematics in arc magmas and implications for crust-mantle differentiation. *Science* 336 (6077), 64–68. doi:10.1126/science.1217313

Lindsay, D .D., Zentilli, M., and Rivera, J .R .D .L. (1995). Evolution of an active ductile to brittle shear system controlling mineralization at the Chuquicamata porphyry copper deposit, northern Chile. *Int. Geol. Rev.* 37 (11), 945–958. doi:10.1080/00206819509465434

Liu, W., Borg, S .J., Testemale, D., Etschmann, B., Hazemann, J .L., and Brugger, J. (2011). Speciation and thermodynamic properties for cobalt chloride complexes in hydrothermal fluids at 35–440 C and 600 bar: an *in-situ* XAS study. *Geochimica Cosmochimica Acta* 75 (5), 1227–1248. doi:10.1016/j.gca.2010.12.002

Liu, W., Migdisov, A., and Williams-Jones, A. (2012). The stability of aqueous nickel (II) chloride complexes in hydrothermal solutions: Results of UV–Visible spectroscopic experiments. *Geochimica Cosmochimica Acta* 94, 276–290. doi:10.1016/j.gca.2012.04.055

Liu, B., Zhang, Z., Cheng, Z., Xie, Q., Turesebekov, A., Nurtaev, B., et al. (2021). Platinum group elements in gabbroic intrusions from the Valerianov Beltau Kurama arc: Implications for Genesis of the Kalmakyr porphyry Cu–Au deposit. *Geol. J.* 56 (1), 46–59. doi:10.1002/gj.3940

Marchev, P., Kaiser-Rohrmeier, B., Heinrich, C., Ovtcharova, M., von Quadt, A., and Raicheva, R. (2005). Hydrothermal ore deposits related to post-orogenic extensional magmatism and core complex formation: The Rhodope Massif of Bulgaria and Greece. *Ore Geol. Rev.* 27, 53–89.

Marini, L., Moretti, R., and Accornero, M. (2011). Sulfur isotopes in magmatic-hydrothermal systems, melts, and magmas. *Rev. Mineral. Geochem.* 73 (1), 423–492. doi:10.2138/rmg.2011.73.14

Marushchenko, L., Baksheev, I., Nagornaya, E., Chitalin, A., Nikolaev, Y .N., and Vlasov, E. (2018). Compositional evolution of the tetrahedrite solid solution in porphyry-epithermal system: A case study of the baimka Cu-Mo-Au trend, chukchi peninsula, Russia. *Ore Geol. Rev.* 103, 21–37. doi:10.1016/j.oregeorev.2017.01.018

Maslennikov, C .C., Maslennikova, S .P., Large, R .R., and Danyushevsky, L .V. (2009). Study of trace element zonation in vent chimneys from the silurian yaman-kasy volcanic-hosted massive sulfide deposit (southern urals, Russia) using laser ablation-inductively coupled plasma mass spectrometry (LA-ICPMS). *Econ. Geol.* 104, 1111–1141. doi:10.2113/gsecongeo.104.8.1111

McDermott, J .M., Ono, S., Tivey, M .K., Seewald, J .S., Shanks, W .C., III, and Solow, A .R. (2015). Identification of sulfur sources and isotopic equilibria in submarine hot-springs using multiple sulfur isotopes. *Geochimica Cosmochimica Acta* 160, 169–187. doi:10.1016/j.gca.2015.02.016

McFall, K .A., Naden, J., Roberts, S., Baker, T., Spratt, J., and McDonald, I. (2018). Platinum- group minerals in the Skouries Cu-Au (Pd, Pt, Te) porphyry deposit. *Ore Geol. Rev.* 99, 344–364. doi:10.1016/j.oregeorev.2018.06.014

McKibben, M .A., and Eldridge, C .S. (1990). Radical sulfur isotope zonation of pyrite accompanying boiling and epithermal gold deposition; a SHRIMP study of the Valles Caldera, New Mexico. *Econ. Geol.* 85 (8), 1917–1925. doi:10.2113/gsecongeo.85.8.1917

McPhail, D. (1995). Thermodynamic properties of aqueous tellurium species between 25 and 350. *Geochimica Cosmochimica Acta* 59 (5), 851–866. doi:10.1016/0016-7037(94)00353-x

Melfos, V., Vavelidis, M., Christofides, G., and Seidel, E. (2002). Origin and evolution of the Tertiary Maronia porphyry copper-molybdenum deposit, Thrace, Greece. *Miner. Deposita* 37 (6), 648–668. doi:10.1007/s00126-002-0277-4

Menant, A., Jolivet, L., Tuduri, J., Loiselet, C., Bertrand, G., and Guillou-Frottier, L. (2018). 3D subduction dynamics: A first-order parameter of the transition from

copper- to gold-rich deposits in the eastern mediterranean region. *Ore Geol. Rev.* 94, 118–135. doi:10.1016/j.oregeorev.2018.01.023

Monecke, T., Monecke, J., Reynolds, T .J., Tsuruoka, S., Bennett, M .M., Skewes, W .B., et al. (2018). Quartz solubility in the H2O-NaCl system: A framework for understanding vein formation in porphyry copper deposits. *Econ. Geol.* 113 (5), 1007–1046. doi:10.5382/econgeo.2018.4580

Murowchick, J .B., and Barnes, H .L. (1986). Marcasite precipitation from hydrothermal solutions. *Geochimica Cosmochimica Acta* 50 (12), 2615–2629. doi:10.1016/0016-7037(86)90214-0

Naden, J., Kilias, S. P., and Darbyshire, D. P. F. (2005). Active geothermal systems with entrained seawater as modern analogs for transitional volcanic-hosted massive sulfide and continental magmato-hydrothermal mineralization: the example of milos island, Greece. *Geol.* 33, 541–544. doi:10.1130/g21307.1

Nestmeyer, M., Keith, M., Haase, K. M., Klemd, R., Voudouris, P., Schwarz-Schampera, U., et al. (2021). Trace element signatures in pyrite and marcasite from shallow marine island arc-related hydrothermal vents, calypso vents, New Zealand, and paleochori bay, Greece. *Front. Earth Sci. (Lausanne).* 9, 641654. doi:10.3389/feart.2021.641654

Ohmoto, H., and Lasaga, A .C. (1982). Kinetics of reactions between aqueous sulfates and sulfides in hydrothermal systems. *Geochimica Cosmochimica Acta* 46 (10), 1727–1745. doi:10.1016/0016-7037(82)90113-2

Ohmoto, H., and Rye, R. O. (1979). "Isotopes of sulfur and carbon," in *Geochemistry of hydrothermal ore deposits chapter 10*. Editor H. L. Barnes. 2nd ed. (Hoboken, New Jersey: John Wiley & Sons), 509–567.

Okrusch, M., and Bröcker, M. (1990). Eclogites associated with high-grade blueschists in the cyclades archipelago, Greece: A review. *Eur. J. Mineral.* 2, 451–478. doi:10.1127/ejm/2/4/0451

Pals, D., and Spry, P. (2003). Telluride mineralogy of the low-sulfidation epithermal Emperor gold deposit, Vatukoula, Fiji. *Mineralogy Petrology* 79 (3), 285–307. doi:10.1007/s00710-003-0013-5

Pe-Piper, G., Christofides, G., and Eleftheriadis, G. (1998). Lead and neodymium isotopic composition of Tertiary igneous rocks of northern Greece and their regional significance. *Acta Vulcanol.* 10, 255–264. doi:10.1017/S0016756898008735

Pe-Piper, G., and Piper, D. J. W. (2002). *The igneous rocks of Greece: The anatomy of an orogen*. Berlin: Gebrüder Borntraeger.

Pe-Piper, G., Piper, D .J., Koukouvelas, I., Dolansky, L .M., and Kokkalas, S. (2009). Postorogenic shoshonitic rocks and their origin by melting underplated basalts: The Miocene of Limnos, Greece. *Geol. Soc. Am. Bull.* 121 (1-2), 39–54. doi:10.1130/B26317.1

Rabbia, O .M., Hernández, L .B., French, D .H., King, R .W., and Ayers, J .C. (2009). The El Teniente porphyry Cu–Mo deposit from a hydrothermal rutile perspective. *Min. Depos.* 44 (8), 849–866. doi:10.1007/s00126-009-0252-4

Redmond, P .B., and Einaudi, M .T. (2010). The Bingham Canyon porphyry Cu-Mo-Au deposit. I. Sequence of intrusions, vein formation, and sulfide deposition. *Econ. Geol.* 105 (1), 43–68. doi:10.2113/gsecongeo.105.1.43

Redmond, P .B., Einaudi, M .T., Inan, E .E., Landtwing, M .R., and Heinrich, C .A. (2004). Copper deposition by fluid cooling in intrusion-centered systems: New insights from the Bingham porphyry ore deposit, Utah. *Geol.* 32 (3), 217–220. doi:10.1130/g19986.1

Reed, M. H., and Palandri, J. (2006). Sulfide mineral precipitation from hydrothermal fluids. *Rev. Mineral. Petrol.* 61, 609–631.

Rees, C. E., Jenkins, W. J., and Monster, J. (1978). The sulphur isotopic composition of Ocean water sulphate. *Geochim. Cosmochim. Acta* 42, 377–381.

Reich, M., Kesler, S .E., Utsunomiya, S., Palenik, C .S., Chryssoulis, S .L., and Ewing, R .C. (2005). Solubility of gold in arsenian pyrite. *Geochimica Cosmochimica Acta* 69 (11), 2781–2796. doi:10.1016/j.gca.2005.01.011

Reich, M., Deditius, A., Chryssoulis, S., Li, J.-W., Ma, C.-Q., Parada, M .A., et al. (2013). Pyrite as a record of hydrothermal fluid evolution in a porphyry copper system: A SIMS/EMPA trace element study. *Geochimica Cosmochimica Acta* 104, 42–62. doi:10.1016/j.gca.2012.11.006

Richards, J .P., and Kerrich, R. (1993). The Porgera gold mine, Papua New Guinea; magmatic hydrothermal to epithermal evolution of an alkalic-type precious metal deposit. *Econ. Geol.* 88 (5), 1017–1052. doi:10.2113/gsecongeo.88.5.1017

Richards, J .P. (2011). Magmatic to hydrothermal metal fluxes in convergent and collided margins. *Ore Geol. Rev.* 40 (1), 1–26. doi:10.1016/j.oregeorev.2011.05.006

Richards, J .P. (2015). The oxidation state, and sulfur and Cu contents of arc magmas: implications for metallogeny. *Lithos* 233, 27–45. doi:10.1016/j.lithos.2014.12.011

Richards, J .P. (2022). Porphyry copper deposit formation in arcs: What are the odds? *Geosphere* 18 (1), 130–155. doi:10.1130/ges02086.1

Ring, U., and Layer, P .W. (2003). High-pressure metamorphism in the aegean, eastern mediterranean: Underplating and exhumation from the late cretaceous until the Miocene to recent above the retreating hellenic subduction zone. *Tectonics* 22 (3). 6-1–6-23. doi:10.1029/2001tc001350

Ring, U., Glodny, J., Will, T., and Thomson, S. (2010). The hellenic subduction system: high- pressure metamorphism, exhumation, normal faulting, and large-scale extension. *Annu. Rev. Earth Planet. Sci.* 38, 45–76. doi:10.1146/annurev.earth.050708.170910

Rivas-Romero, C., Reich, M., Barra, F., Gregory, D., and Pichott, S. (2021). The relation between trace element composition of Cu-(Fe) sulfides and hydrothermal alteration in a porphyry copper deposit: Insights from the Chuquicamata underground mine, Chile. *Minerals* 11 (7), 671. doi:10.3390/min11070671

Roedder, E. (1971). Fluid inclusion studies on the porphyry-type ore deposits at Bingham, Utah, Butte, Montana, and Climax, Colorado. *Econ. Geol.* 66 (1), 98–120. doi:10.2113/gsecongeo.66.1.98

Román, N., Reich, M., Leisen, M., Morata, D., Barra, F., and Deditius, A .P. (2019). Geochemical and micro-textural fingerprints of boiling in pyrite. *Geochimica Cosmochimica Acta* 246, 60–85. doi:10.1016/j.gca.2018.11.034

Roussos, N. (1993). *Geological map of Greece, lemnos island sheet*, 1. Institute of Geology and Mineral Exploration of Greece.

Rye, R .O. (2005). A review of the stable-isotope geochemistry of sulfate minerals in selected igneous environments and related hydrothermal systems. *Chem. Geol.* 215 (1-4), 5–36. doi:10.1016/j.chemgeo.2004.06.034

Schaarschmidt, A., Klemd, R., Regelous, M., Voudouris, P .C., Melfos, V., and Haase, K .M. (2021a). the formation of shoshonitic magma and its relationship to porphyry-type mineralisation: the maronia pluton in NE Greece. *Lithos* 380, 105911. doi:10.1016/j.lithos.2020.105911

Schaarschmidt, A., Haase, K .M., Klemd, R., Keith, M., Voudouris, P., Alfieris, D., et al. (2021b). Boiling effects on trace element and sulfur isotope compositions of sulfides in shallow-marine hydrothermal systems: Evidence from Milos Island, Greece. *Chem. Geol.* 583, 120457. doi:10.1016/j.chemgeo.2021.120457

Schauble, E .A. (2004). Applying stable isotope fractionation theory to new systems. *Rev. mineralogy Geochem.* 55 (1), 65–111. doi:10.2138/gsrmg.55.1.65

Schirra, M., and Laurent, O. (2021). Petrochronology of hydrothermal rutile in mineralized porphyry Cu systems. *Chem. Geol.* 581, 120407. doi:10.1016/j.chemgeo.2021.120407

Schneider, C .A., Rasband, W .S., and Eliceiri, K .W. (2012). NIH image to ImageJ: 25 years of image analysis. *Nat. Methods* 9 (7), 671–675. doi:10.1038/nmeth.2089

Seal, R .R. (2006). Sulfur isotope geochemistry of sulfide minerals. *Rev. mineralogy Geochem.* 61 (1), 633–677. doi:10.2138/rmg.2006.61.12

Seedorff, E., Dilles, J .H., Proffett, J .M., Einaudi, M .T., Zurcher, L., Stavast, W .J., et al. (2005). Porphyry deposits: Characteristics and origin of hypogene features. *Econ. Geol.* 1. 251–298. doi:10.5382/AV100.10

Sillitoe, R .H. (1994). Erosion and collapse of volcanoes: Causes of telescoping in intrusion- centered ore deposits. *Geol.* 22 (10), 945–948. doi:10.1130/0091-7613(1994)022<0945:eacovc>2.3.co;2

Sillitoe, R .H. (2010). Porphyry copper systems. *Econ. Geol.* 105 (1), 3–41. doi:10.2113/gsecongeo.105.1.3

Simmons, S .F., White, N .C., and John, D .A. (2005). Geological characteristics of epithermal precious and base metal deposits. *Econ. Geol.* 100. 1. doi:10.5382/AV100.16

Smith, D .J., Naden, J., Jenkin, G .R .T., and Keith, M. (2017). Hydrothermal alteration and fluid pH in alkaline-hosted epithermal systems. *Ore Geol. Rev.* 89, 772–779. doi:10.1016/j.oregeorev.2017.06.028

Sotiropoulos, S., Kamberis, E., Triantaphyllou, M .V., and Doutsos, T. (2003). Thrust sequences in the central part of the External Hellenides. *Geol. Mag.* 140 (6), 661–668. doi:10.1017/s0016756803008367

Sykora, S., Cooke, D .R., Meffre, S., Stephanov, A .S., Gardner, K., Scott, R., et al. (2018). Evolution of pyrite trace element compositions from porphyry-style and epithermal conditions at the Lihir gold deposit: Implications for ore Genesis and mineral processing. *Econ. Geol.* 113 (1), 193–208. doi:10.5382/econgeo.2018.4548

Syverson, D .D., Ono, S., Shanks, W .C., and Seyfried, W .E., Jr (2015). Multiple sulfur isotope fractionation and mass transfer processes during pyrite precipitation and recrystallization: an experimental study at 300 and 350°C. *Geochimica Cosmochimica Acta* 165, 418–434. doi:10.1016/j.gca.2015.06.022

Tian, Y., Etschmann, B., Liu, W., Borg, S., Mei, Y., Testemale, D., et al. (2012). Speciation of nickel (II) chloride complexes in hydrothermal fluids: *In situ* XAS study. *Chem. Geol.* 334, 345–363. doi:10.1016/j.chemgeo.2012.10.010

Tostevin, R., Turchyn, A .V., Farquhar, J., Johnston, D .T., Eldridge, D .L., Bishop, J .K., et al. (2014). Multiple sulfur isotope constraints on the modern sulfur cycle. *Earth Planet. Sci. Lett.* 396, 14–21. doi:10.1016/j.epsl.2014.03.057

Tranos, M. D. (2009). Faulting of Lemnos Island; A mirror of faulting of the North Aegean Trough (Northern Greece). *Tectonophysics* 467 (1–4), 72–88.

Ulrich, T., and Mavrogenes, J. (2008). An experimental study of the solubility of molybdenum in H2O and KCl–H2O solutions from 500˚C to 800˚C, and 150 to 300 MPa. *Geochimica Cosmochimica Acta* 72 (9), 2316–2330. doi:10.1016/j.gca.2008.02.014

van Hinsbergen, D .J .J., Hafkenscheid, E., Spakman, W., Meulenkamp, J., and Wortel, R. (2005). Nappe stacking resulting from subduction of oceanic and continental lithosphere below Greece. *Geol.* 33 (4), 325–328. doi:10.1130/g20878.1

Vigneresse, J.-L., Truche, L., and Richard, A. (2019). How do metals escape from magmas to form porphyry-type ore deposits? *Ore Geol. Rev.* 105, 310–336. doi:10.1016/j.oregeorev.2018.12.016

Voudouris, P., Mavrogonatos, C., Spry, P., Baker, T., Melfos, V., Klemd, R., et al. (2019a). Porphyry and epithermal deposits in Greece: An overview, new discoveries, and mineralogical constraints on their Genesis. *Ore Geol. Rev.* 107, 654–691. doi:10.1016/j.oregeorev.2019.03.019

Voudouris, P., Baksheev, I .A., Mavrogonatos, C., Spry, P .G., Djiba, A., Bismayer, U., et al. (2019b). Tourmaline from the Fakos porphyry-ep- ithermal Cu-Mo-Au-Te prospect, Limnos island, Greece: mineral-chemistry and genetic implications. *Bull. Geol. Soc. Greece* 7, 329–330.

Voudouris, P. (2006). A comparative mineralogical study of Te-rich magmatic-hydrothermal systems in northeastern Greece. *Mineralogy Petrology* 87 (3-4), 241–275. doi:10.1007/s00710-006-0131-y

Voudouris, P., Velitzelos, D., Velitzelos, E., and Thewald, U. (2007). Petrified wood occurences in Western thrace and Limnos island: mineralogy, geochemistry and depositional environment. *geosociety.* 40, 238–250. doi:10.12681/bgsg.16543

Wallier, S., Rey, R., Kouzmanov, K., Pettke, T., Heinrich, C. A., Leary, S., et al. (2006). Magmatic fluids in the brecciahosted epithermal Au-Ag deposit of Rosia Montana, Romania. *Econ. Geol.* 101 (5), 923–954.

Whitney, D. L., and Evans, B. W. (2010). Abbreviations for names of rock-forming minerals. *Am. Mineral.* 95 (1), 185–187.

Zhang, Z .C., and Mao, J .W. (1995). Geology and geochemistry of the dongping gold telluride deposit, heibei province, north China. *Int. Geol. Rev.* 37 (12), 1094–1108. doi:10.1080/00206819509465441

Zhang, Q., Liu, Y., He, M., Bai, J., Xu, W., and Zhao, C. (2018). Ore prospecting model and targets for the Dashuigou tellurium deposit, Sichuan Province, China. *Acta Geochim.* 37 (4), 578–591. doi:10.1007/s11631-018-0271-x